Louisiana Tech University

Louisiana Tech Digital Commons

Fall 11-17-2018

Effective Magnetic and Electric Response of Composite Materials

Mona Hassan Alsaleh

Follow this and additional works at: https://digitalcommons.latech.edu/dissertations

Part of the Electromagnetics and Photonics Commons, Other Electrical and Computer Engineering Commons, Other Engineering Commons, Other Engineering Science and Materials Commons, Other Materials Science and Engineering Commons, and the Other Physics Commons

Fall 11-17-2018

Effective Magnetic and Electric Response of Composite Materials

Mona Hassan Alsaleh

EFFECTIVE MAGNETIC AND ELECTRIC RESPONSE OF

COMPOSITE MATERIALS

by

Mona H. Alsaleh, B.S., M.S.

A Dissertation Presented in Partial Fulfillment
of the Requirements of the Degree
Doctor of Philosophy

COLLEGE OF ENGINEERING AND SCIENCE
LOUISIANA TECH UNIVERSITY

November 2018

LOUISIANA TECH UNIVERSITY

THE GRADUATE SCHOOL
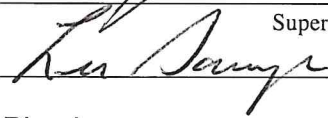
SEPTEMBER 27, 2018
<div align="right">Date</div>

We hereby recommend that the dissertation prepared under our supervision by Mona Hassan Alsaleh B.S., M.S.

entitled

Effective Magnetic and Electric Response of Composite Materials

be accepted in partial fulfillment of the requirements for the Degree of Doctor of Philosophy in Engineering (Concentration in Physics)

<div align="right">Supervisor of Dissertation Research</div>

<div align="right">Head of Department</div>

Physics
<div align="right">Department</div>

Recommendation concurred in:

Erica P. Murray

S. Bivauore

Advisory Committee

Approved:

Director of Graduate Studies

Dean of the College

Approved:

Dean of the Graduate School

ABSTRACT

Metamaterials (MMs) are nanocomposite materials consisting of metal-dielectric resonators much smaller in size than the wavelength of the incident light. Common examples of metamaterials are based on split ring resonators (SRRs), parallel wires or strips and fishnet structures. These types of materials are designed and fabricated in order to provide unique optical responses to the incident electromagnetic radiation that are not available in naturally existing materials. The MMs can exhibit unusual properties such as strong magnetism at terahertz (THz) and optical frequencies. Add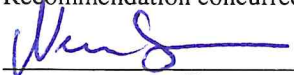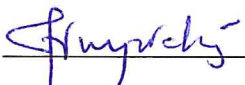itionally, negative index materials (NIMs) can provide negative index of refraction which can be used in many applications including invisibility cloaking devices and superlenses capable of overcoming the diffraction limit of light. Furthermore, NIMs manifest reversal of optical laws such as Snell's law, the Doppler effect and Cerenkov radiation.

This dissertation demonstrates comprehensive analytical and theoretical studies of the magnetic and electric susceptibilities of prospective two dimensional MMs including metallic parallel strips and bowtie resonators. Accurate analytical theories are developed to describe the diamagnetic response of a pair of metallic nanostrips separated by a dielectric material using the transmission line theory, and of metallic bowtie MMs through a high frequency LZ circuit model. These theoretical models were compared to exact numerical simulations based on the finite difference frequency domain (FDFD) Comsol Multiphysics software. The magnetic response for both systems was extracted numerically

iii

by applying the polarization current approach and found to be in excellent agreement with the analytical theory. Our results show that strong optical magnetism can be realized by reducing the size of the resonators; however, the scaling breaks down at high frequencies where a clear saturation in the magnetic resonance frequency is manifested in both systems under investigation. Moreover, the proposed NIMs designs are shown to exhibit negative index of refraction in the case of metallic and semiconductor based strips resonators. A record high figure of merit (FOM) of -0.9 has been demonstrated for double negative index material (demonstrating simultaneously negative permittivity and permeability). The local electromagnetic response of the NIMs was extracted using two competing approaches, namely the field averaging and inverse methods. These methods have shown consistent results, specifically with respect to the predicted magnetic susceptibility, and thus have testified that the proposed magnetic resonance designs can lead to prospective high fidelity NIMs that should be implemented in practice.

As a separate effort related to this thesis, a ceramic material (i.e. yttria stabilized zirconia (YSZ)) was used to fabricate a NO_x sensor. Since diesel engines emits more particulates and NO_x exhaust gases compared to gasoline engine, a NO_x sensor is required to monitor emission in diesels vehicle. The proposed NO_x sensor consists of a porous electrolyte and dense electrode. The porosity of YSZ is studied with direct Archimedes measurements and through scanning electron microscopy (SEM) of the YSZ at different firing temperatures. The electrochemical performance of NO_x sensor was finally examined and verified by using impedance spectroscopy (IS).

APPROVAL FOR SCHOLARLY DISSEMINATION

The author grants to the Prescott Memorial Library of Louisiana Tech University the right to reproduce, by appropriate methods, upon request, any or all portions of this Dissertation. It is understood that "proper request" consists of the agreement, on the part of the requesting party, that said reproduction is for his personal use and that subsequent reproduction will not occur without written approval of the author of this Dissertation. Further, any portions of the Dissertation used in books, papers, and other works must be appropriately referenced to this Dissertation.

Finally, the author of this Dissertation reserves the right to publish freely, in the literature, at any time, any or all portions of this Dissertation.

Author _____

Date _____

DEDICATION

This dissertation is dedicated to everyone who has supported, encouraged and helped me to accomplish my PhD work.

TABLE OF CONTENTS

LIST OF FIGURES

LIST OF TABLES

ACKNOWLEDGMENTS

I am very thankful for my advisor Dr. Dentcho Genov for his patience, especially at the beginning of my PhD since I was not sure if I would be able to continue my studies. I really appreciate him for accepting me in his group without me having any previous knowledge in numerical simulations and physics in general. Also, I would like to thank Dr. Erica Murray for being my co-advisor and to let me work in her lab. She accepts students' mistakes so they can learn from their mistakes. Additionally, I am really grateful and thankful for Dr. Neven Simicevic for listening to me and helping me throughout my PhD studies. I would also like to thank Dr. Arun and Dr. Sandra for serving as my committee members.

A special thanks to Raj Kumar Vinnakota who has been always there to help me and support me at any time related to PhD work, conferences, presentations, or even in class. I also want to thank my family who allowed me to continue studying in the USA. My deepest thanks to my brother who always encouraged me and supported me.

CHAPTER 1

INTRODUCTION

1.1   Metamaterials

During the past few decades there have been great efforts in developing new types of optical materials that could manipulate light in a desired manner; these materials are commonly referred to as designed materials (DMs). The key goals for developing such materials are to lift current limitations in the responses and capabilities of electromagnetic devices which are set by the available naturally existing materials used to build them. The DMs are synthesized or manufactured at the atomic or nano-length scales and can exhibit electromagnetic responses far beyond those available in nature. There are many types of designed materials with the photonic crystals (PCs) and metamaterials (MMs), two particular examples. This dissertation research focuses on designing metamaterial structures that can provide electromagnetic response that are substantially different compared to the optical responses of ordinary media [1, 2].

The electromagnetic metamaterials (MMs) are composed of artificial atoms (i.e. metal-dielectric elements) in the same way as the traditional materials consist of atoms. Usually, the MMs are periodic arrangements of resonator structures with the basic structural element defining a unit cell that has to be much smaller than the wavelength of interest. These structural elements are in the form of split ring resonators (SRRs), fishnet

structure, parallel wires or slabs arranged in large 1D, 2D or 3D arrays (see Figure 1-1) [2, 3, 4, 5, 6, 7, 8]. Metamaterials gain their properties from their internal geometrical structure rather than the intrinsic properties of the chemical constituents [2, 9]. Although metamaterials are composed of highly inhomogeneous inclusions, their electromagnetic responses to the incident light can be expressed in terms of homogenized effective electric permittivity ε and magnetic permeability μ.
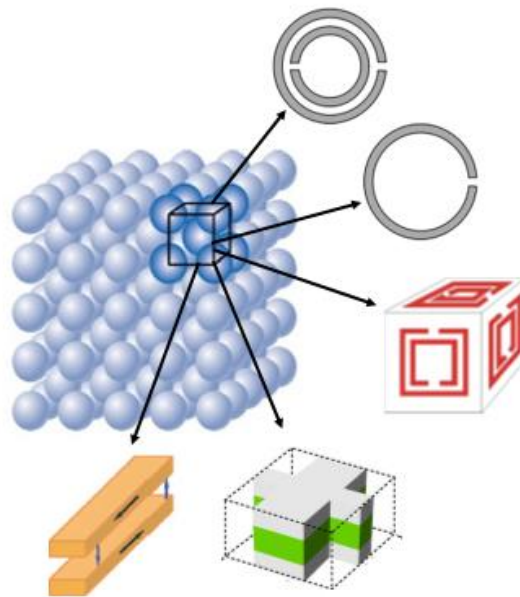
Figure 1-1: The metamaterials are periodic arrangements of unit cells each consisting of designed resonator structure [5, 6, 17, 18].

When considering the history of metamaterials, it is important to mention that since B.C.E., metal inclusions into glass (stained glasses) has been used to control color. For instance, it was found that adding reduced or oxidized copper into the glass results in stained glasses with either red or blue colors, respectively. One of the most famous example of such metalized glasses is the Lycurgus Cup exhibited in the British Museum (Figure 1-

2). This cup was made in the fourth century A.D. during the Roman Empire [19]. The cup appears green in Figure1-2 (a) when the light is reflected off the surface of the cup; however, when the light is transmitted through the cup, the cup looks red (Figure 1-2 (b)). The Lycurgus cup has a remarkable behavior which results from introducing colloidal gold and silver nanoparticles into the glass.

Figure 1-2: The Lycurgus cup appears (a) green when light is reflected off the surface of the cup, and (b) red when the light is transmitted through the cup [19].

Apart from the Lycurgus cup, people based on trial and error have produced a large variety of stained glasses by incorporating nanosize metallic inclusions within the molted glass. In the eighth century, Jabir ibn Hayyan discussed the manufacturing of colored glass and the technique for coloring gemstones in his book '*The book of the Hidden Pearl*' which is arguably considered the first book on man-made MMs [19].

In relatively modern times long before the term "metamaterials" emerged in science, there have been many attempts at producing artificial MMs and explaining their properties. In 1898, Bose developed the first artificial chiral material by using pieces of twisted jute in subwavelength sizes [20]. Later in 1904, J.C.M. Garnett in his paper

described how the colors occurred and changed within glasses when gold or silver films were annealed into nanoparticles and dispersed throughout soda glass. His study was based on the Drude model which describes the optical properties of free electron in metals [21]. In 1908, the well-known Mie scattering theory was developed providing an exact treatment of scattering of light by metallic or dielectric spheres. This theory calculates the scattering of the incident light providing explicit formulation for the electric and magnetic fields inside and outside of the sphere [22]. All these previous works represent major efforts in developing optical materials and explaining the behavior of nanoparticles and are thus considered to be fundamental turning points in the history of metamaterials.

The emergence of modern optical metamaterials started in the late 60s. The most inspiring works of modern metamaterials are the three seminal paper by Victor Veselago in 1967 [23], David Smith in 2000 [24] and John Pendry in 2000 [11]. Veselago developed the theoretical framework of negative index materials, claiming that these types of materials would provide unusual phenomena in which the electric field, magnetic field and the wave vector of light propagate in the opposite direction compared to that in positive index materials. Additionally, he showed that to have negative index material, it is required for the permittivity and permeability to be concurrently negative within a common frequency band. In such left handed materials (LHMs), many unique properties are predicted to take place such as reversal of Snell's Law and reversal of the Doppler and Cerenkov effects. Veselago's work was ignored for a very long time due to the absence of naturally existing double negative material (i. e. materials with both $\varepsilon < 0$ and $\mu < 0$), which made negative index of refraction a near impossibility. His ideas were not realized experimentally until 2000, when Smith *et al*. fabricated the first NIMs operating in the

microwave frequency regime [24]. Since this founding work there has been an enormous attention to NIMs by scientists working in optics, physics, electromagnetism, material science and engineering. This strong interest was further inflamed after John Pendry predicted that NIMs can be used to make perfect lenses allowing imaging with resolution beyond the conventional diffraction limit of light [6, 18, 9, 25, 26].

The electromagnetic response of metals at optical frequencies is drastically different from those at lower frequencies where the permittivity of metals is highly negative so that they behave as "perfect" conductors. At frequencies close or above the plasma frequency which of noble metals is situated in the optical range, they behave as dielectrics. As a result, metallic nanostructures can exhibit morphological plasmon resonances and are transparent at high frequencies. To achieve similar behavior at low (microwave) frequencies designed composites materials have been proposed based on sparse arrays of metal wires [9, 10, 26, 27]. Some ferromagnetic materials show negative magnetic susceptibilities at microwave frequencies as well; however, the magnetic response is very weak in the THz and nonexistent in the optical frequency range [28]. The resonance nature of the electric response of metallic structures at optical frequencies can provide excitations of strong closed currents and thus open the possibility for achieving negative permeability and negative permittivity within a common frequency range [10]. Following this concept, researchers have designed and fabricated metamaterials with simultaneously negative electric and magnetic responses. A brief history of the most inspiring works in the field of MMs follows.

In 1999, Pendry was the first to propose a negative index material consisting of periodic metallic thin wires to provide a negative permittivity ($\varepsilon < 0$) and coupled to split

ring resonators (SRRs) that support closed currents and strong diamagnetic moments ($\mu <$ 0). The lattice constant of his structure was much smaller than the excitation wavelength of light; hence, the system behaved as a homogeneous material exhibiting negative index of refraction [3], [29]. Based on Pendry's design, in 2000, Smith *et al*. fabricated and characterized the first NIM to operate in the microwave regime [24]. Similar work was done by Shelby *et al*. in 2001 [30], [31]. The proposed design again relies on split ring resonators (SRR) to achieve negative permeability and wire strips centered on the SRRs to provide a negative permittivity (see Figure 1-3). This experiment showed a negative index of refraction at GHz frequencies.

Figure 1-3: Bulk negative index materials with the unit cell consisting of SRR combined with the metallic wire [30].

These founding works thus validated the ideas behind negative index materials (NIMs) for microwaves. Later, researchers were able to demonstrate negative permeability at THz frequencies by shrinking the size of the SRRs to a few micrometers [32]. At the same time, Linden *et al*. [33] fabricated a single ring resonator made of copper and by reducing the size of the ring down to the nanometer length scale they were able to demonstrate magnetic response up to 100 THz.

While all initial efforts were focused on developing metamaterials' structures consisting of metallic SRRs, it was recognized that this particular design cannot be scaled down to provide magnetism at optical frequencies. Hence, the research efforts shifted into seeking alternative and simpler designs that can be easily fabricated and experimentally characterized.

Podolskiy *et al*. [7] showed that a simple structure based on pairs of metal nanorods is capable of demonstrating negative permeability and negative index of refraction at optical frequencies.   Then by following an identical design, Shalaev *et al*. [6] experimentally demonstrated the first optical metamaterial with NIR, the proposed structure consists of parallel gold nanorods separated by a dielectric material as shown in Figure 1-4. This structure showed an effective negative permeability at 200 THz.
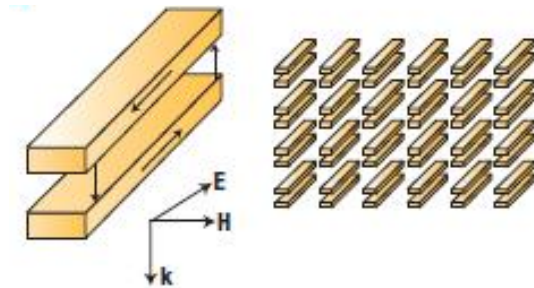
Figure 1-4: Optical negative index material consisting of array of pair of nanorods [6].

Only in 2008, the first true bulks NIM based on alternative layers of silver and magnesium fluoride in the form of a fishnet structure, shown in Figure 1-5, was successfully developed and tested, providing a direct evidence of negative refraction at near infrared frequencies. This structure had a figure of merit (FOM), the ratio between the

real and imaginary part of the refraction index, surpassing -3.5, which remains the record holder as of today [8].
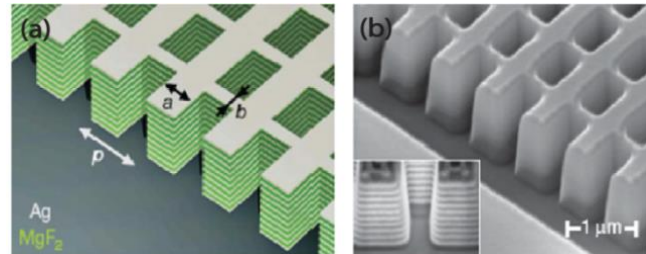
Figure 1-5: Fishnet type bulk negative index materials in the optical range [8] (a) schematics of 21 layer fishnet structure and (b) SEM image of the fabricated fishnet structure.

The large number of important potential applications of metamaterials continues to drive rapid growth of optical research in the field. In the next section, we discuss the most important applications of metamaterials, applicable to optics.

1.1.1   Applications of Metamaterials

There are many fascinating applications of metamaterials such as metamaterials antennas, biosensors, optical nanolithography, nanocircuits and metamaterials also used as a medium for the transformation of optics. The transformation optics approach is used to precisely control the light's flow in a desirable way by tailoring the properties of the complex materials consisting of discrete elements with pre-set magnetic permeability and electric permittivity. Metamaterials allows realization of many attractive optical phenomena and devices such as cloaking devices that conceal the object to be invisible. Metamaterials with negative index of refraction can be used to develop superlenses capable of imagining objects beyond the diffraction limit of light. We first take the invisible cloak to present the basic concept of transformation optics as illustrated in Figure 1-6(a). Then,

we will describe how NIMs can be used to develop superlenses by amplifying the subwavelength details of the object.
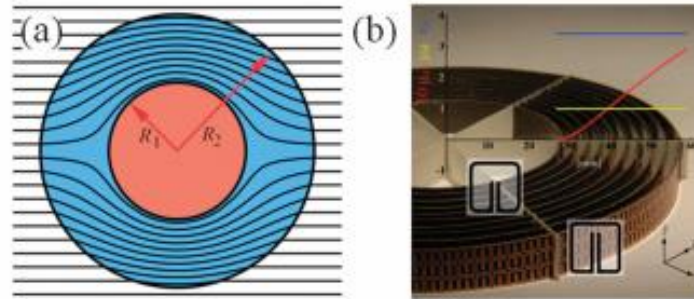
Figure 1-6: (a) Schematics of two- dimensional electromagnetic cloak, (b) Fabricated microwave cloak made of SRRs [34, 35].

An electromagnetic clock conceals any object contained in a given volume of space so that scattering of light from the object is minimized and external observers are thus unaware of the hidden object. To achieve this goal, one mathematically stretches a region of space opening a circular void for $r < R_1$. The initial uniform light rays are then partially deflected by a metamaterial shell in the region where $R_1 < r < R_2$, so the light rays are conformally guided around the object instead of striking its surface. All light rays in the region $r > R_2$ are thus un-altered. There are no light rays that can get into or interact with the core region, nor do any waves get out of the core region. No matter what objects are placed inside the core, it is perceived to an observer that nothing exists since any waves attempting to penetrate the core region are smoothly guided around the concealed object by the cloak and emerge traveling in the same direction and with the same phase as if it had passed through empty space. Thus, nothing exists for the observer, that is, the object is concealed or cloaked. The distortion of space can be tracked by certain coordinate

transformations which effectively introduced in the Maxwell's equations a position dependent effective anisotropic permittivity and permeability. If these are reproduced in practice, the system will behave as the desired cloak. The first proof-of principle was built in the form of ten cylindrical layers of SRRs working over a band of microwave frequencies. The SRRs have different geometrical parameters (Figure. 1-6 (b)), therefore realizing the predesigned spatial distribution of anisotropic permittivity and permeability [34, 35, 36].

The superlens is one of the most famous applications of negative index materials. This kind of lens is different than ordinary lenses since it can provide a perfect resolution of the object preserving in the image features smaller than the diffraction limit of light $\lambda/2$. A small size object is represented by evanescent waves that carry information about the object's microscopic structures. These waves decay exponentially in free space and all details of the subwavlength information for the object are lost at the image plane. Pendry [11, 34] showed that NIM can work as a perfect lens by recovering all the lost information. This is accomplished as the evanescent waves are amplified as they pass through a negative index material slab perfectly restoring the object at the focus plane as shown in Figure 1-7.
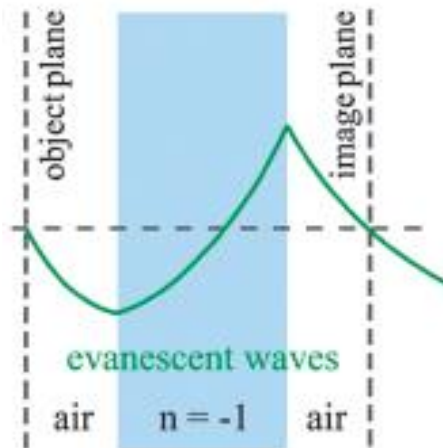
Figure 1-7: The NIM slab can amplify evanescent waves leading to perfect imaging at the image plane [34].

1.2   Dissertation Organization

This dissertation is organized as follows. In Chapter 2, we provide a theoretical study of magnetic plasmons in two dimensional metal-dielectric resonators. We have developed an analytical theory for the magnetic susceptibility of parallel stripes and bowtie metamaterials. We have performed full wave calculations utilizing COMSOL Multiphysics commercial software to extract the magnetic response of the systems. The magnetic response of both systems is calculated utilizing the current polarization approach and compared to the developed analytical theory. The fundamental physical reasons behind the observed saturation in the magnetic response at high frequencies are explained using RLC circuit models.

In Chapter 3, we design negative index metamaterials based on the resonant structures studied in the preceding chapter. Two separate methods are used for extracting the magnetic permeability and electric permittivity of the systems, namely the local field

averaging method and the inverse method. The proposed designs based on periodic arrangements of parallel microstrips immersed into a dielectric host are shown to be adequate for the development of NIMs with high figure of merit (FOM).

In Chapter 4, we have used ceramic material i.e. yttria stabilized zirconia (YSZ) as an electrolyte of NO_x sensor. The porosity of YSZ electrolyte pellets was studied using Archimedes measurement and scanning electron microscopy (SEM) at varying firing temperatures. The NO_x sensor was fabricated by attaching parallel gold wires to electrolyte pellet and coated with layers of YSZ slurry at room temperature. The final NO_x sensor structure consists of two gold wires embedded between two layers of YSZ. Two sensors fired at 1050℃ and 1100℃ have been fabricated. The performance of the NO_x sensors was studied through Electrochemical Impedance Spectroscopy (EIS). Two types of plot were used for the analysis, Nyquist plot and the phase angle O_2 dependence plot. Nyquist plot was used to examine the influence of temperature, NO, O_2, and adding oxygen to NO. Our analyses show that increasing the temperature, Oxygen, and NO concentrations decreases the low frequency arc, which increases the sensitivity of the NO_x sensor. A phase angle oxygen dependence analyses shows that the NO_x sensor is less sensitive to the Oxygen concentration but have higher sensitivity to NO.

CHAPTER 2

SATURATION OF MAGNETIC RESPONSE IN METAMATERIALS

2.1 Magnetic Response of Materials

Materials react differently to the external electromagnetic field and their response is based on their atomic and molecular structure and on the net magnetic field associated with it. The magnetic moment of atoms is caused by the motion of electrons and their spin. In most materials, electrons spins are randomly distributed due to thermal agitation which results in weak or nonexistent magnetization. Thus, the net magnetic field associated with the atoms is zero. However, special materials do exist where the spins can be partially aligned providing a net magnetization. These materials are classified as diamagnetic, paramagnetic or ferromagnetic with the magnetic response of the materials described by the magnetic susceptibility χ_m.

Diamagnetic materials manifest weak negative susceptibility and are repelled by an external magnetic field. Examples of the diamagnetic materials include silver, gold and copper.

Paramagnetic materials manifest weak positive susceptibility and are attracted by an external magnetic field example for paramagnetic materials includes lithium, magnesium, and tantalum.

Ferromagnetic materials have a large positive susceptibility and demonstrate strong attraction to an external magnetic field. Example for ferromagnetic materials are Iron, nickel, and cobalt [37, 38, 39, 40].

For achieving optical negative index materials which require not only negative permittivity but also negative permeability (i.e. diamagnetic response) at THz and optical range frequencies, scientists must engineer metamaterials with subwavelength sizes constituent elements that mimic the magnetic response of atoms but at a much higher strength.

2.1.1 Magnetic Response of Metamaterials at High Frequencies

Most naturally existing materials weakly couple to the magnetic field of the impinging light at the optical frequency range, thus their magnetic permeability equals to one [10]. At GHz frequencies, split ring resonators based metamaterials has been suggested by Pendry to provide negative permeability [3]. The split ring resonators can be regarded as a simple LC resonant circuit with resonance frequency $\omega_0 = 1/\sqrt{LC}$, where the metal rings form the inductive and the dielectric gaps act as capacitive elements [4]. When electromagnetic wave is impinging on the SRRs, the magnetic field component perpendicular to the plane of the rings induces a circular current which itself induces a magnetic moment in the structure. For frequencies below the resonance frequency, the induced current in the SRR increases as the frequency of the applied magnetic field increases resulting in positive paramagnetic response. However, as the frequency of the external magnetic field increases and reaches the LC resonance frequency, the current eventually begins to lag and changes its sign, resulting in negative diamagnetic response. The various designs of SRRs can be viewed as metamaterials consisting of artificial

magnetic atoms [40, 41].   The general resonant form of the frequency dependent permeability for SRR is given as

$$\mu_r(\omega) = 1 - \frac{F\omega^2}{\omega^2 - \omega_0^2 + i\omega\omega_t} \ ,$$ **Eq. 2-1**

where F is the fractional volume of the unit cell occupied by SRR, ω_0 is the resonance frequency, and ω_t is the resistive damping frequency [3].

After Pendry proved theoretically that strong diamagnetic response can be achieved using SRRs, Smith *et al.* demonstrated this effect experimentally in the microwave region [24].   Since these founding works, there have been many efforts aimed at better understanding the MMs' behavior at low and high frequencies. The majority of the fabricated and designed metamaterials' structures comprised of metallic (SRRs) separated by dielectric materials with structural size much smaller than the excitation wavelength of light [3, 24, 31-33, 42-44]. Progress in metamaterials has been rapid since many researchers determined to extend MMs to THz, infrared and visible bands.

Smith's SRRs had a diameter of several millimeters and scaling down the size of SRRs leads to a diamagnetic response at higher frequencies. Using this scaling technique was crucial to push the resonance frequency from 1 THz up to 100 THz frequency [32], [33]. However, the scaling approach of SRRs breaks down at optical frequencies [45], [46]. Hence, it was necessary to design other improved and simplified resonating structures, which can be easily fabricated and experimentally characterized. This was achieved by using pairs of metallic strips or wires separated by dielectric materials [6, 7, 47, 48]. The main reason to replace the SRRs by a pair of wires or strips is the possibility of demonstrating a diamagnetic response with just a monolayer of resonators [48]. Using parallel nanogold strips shows diamagnetic response at visible frequency range [6]. The

parallel slabs system also shows saturation for the magnetic resonance frequency as the size of the metallic strips is scaled down to nanometers [48]. There are many publications that attempt to phenomenologically explain the saturation effects pertaining to the scaling approach with the main ideas having to do with the finite kinetic energy of the conduction electron in small size of metal elements [4, 45, 46, 48].

In this chapter, we present a transmission line theory to model the magnetic response of a pair of silver slabs separated by a dielectric material. Additionally, by utilizing LZ circuit model, we provide an analytical model for the magnetic susceptibility and magnetic frequency resonance for silver bowtie nanostructures separated by dielectric material. The predictions of the analytical models were then compared to exact numerical simulations obtained utilizing finite different frequency domain (FDFD) Comsol Multiphysics software showing excellent correspondence.

2.2   Parallel Slabs Metamaterials

2.2.1   Theory of Magnetic Response of Parallel Slabs Metamaterials

To obtain the magnetic susceptibility of parallel slabs metamaterials, see Figure 2-1(a), we utilize the transmission line approach where the system is modeled with an equivalent circuit shown in Figure 2-1(b).
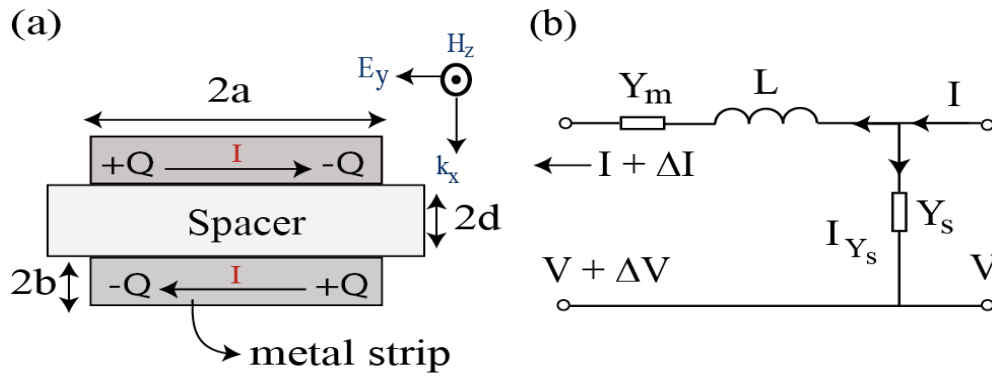
Figure 2-1: (a) Schematic of the metal nanostrips metamaterial element. (b) Generalized (low/ high) transmission line circuit model with Y_m and Y_s are the metal and the spacer admittance, L is the inductance.

The circuit is composed of metallic and spacer admittances (Y_m, Y_s), inductance L and a source electromotive force provided by the external magnetic field. The parallel slabs system consists of silver slabs separated by a glass with the geometrical outline illustrated in Figure 2-1(a). The system is illuminated from the top with a harmonic TM-polarized wave with the magnetic field $\vec{H}(x,t) = \hat{z}H_0\, e^{-ik_0 x}\, e^{i\omega t}$, where $k_0 = \omega/c$ is the wave vector in free space and c is the speed of light. The magnetic field excites an antiparallel current in the structure which drives it diamagnetic response. To model the system, we consider a small segment along the metal strips with length Δy for which the Kirchhoff's current and voltage laws are written as

$$\Delta I\ = I_{Y_s} = Y_s V \Delta y,$$
$$\Delta V = \Delta V_{Y_m} + \Delta V_L + \Delta V_B\,,$$

Eq. 2-2

where $Y_s = i\omega C$, C is the capacitance per unit length, $\Delta V_{Y_m} = I Z_m \Delta y$ and $\Delta V_L = L(\partial I/\partial t)\Delta y$ are the potential drops due to the metal strips admittance and inductance. We consider the harmonic oscillation of the current $\vec{I}(y,t) = \hat{y}I_0(y)e^{i\omega t}$, where ω is the angular frequency then the Kirchhoff's voltage law follows as

$$\Delta V = I Z_m \Delta y + i\omega L I \Delta y + \Delta V_B \,, \qquad\qquad \text{Eq. 2-3}$$

where $\Delta V_B = \partial \phi_B / \partial t$ is the electromotive force generated by incident magnetic field $\vec{H}$.

The magnetic flux $\phi_B = \int B.\,da$ over the resonator can be estimated as

$$\Delta V_B = i\omega\mu_0 \Delta y(4b + 2d)\mathrm{sinc}[(2b + d)k_0]H_0 e^{i\omega t} \,, \qquad\qquad \text{Eq. 2-4}$$

where μ_0 is the permeability of free space. Substituting ΔV_B back into Eq. 2-3 and considering the limits $\Delta V/\Delta y \to \partial V/\partial y$ and $\Delta I/\Delta y \to \partial I/\partial y$, we can decouple the two governing equations by differentiation. Finally, we arrive at the transmission line equation

$$\frac{d^2 I(y)}{dy^2} = -k^2 I(y) - v^2 H_0, \qquad\qquad \text{Eq. 2-5}$$

where $k^2 = LC\omega^2 - i\omega C Z_m$ and $v^2 = \mu_0 C\omega^2 (4b + 2d)\mathrm{sinc}[(2b + d)k_0]$. The transmission line circuit's elements per unit length are derived in Appendix A.1 and given as

$$Z_m = \frac{1}{i\omega\epsilon_0\epsilon_m b l_z}, \quad C = \epsilon_0\epsilon_s \frac{l_z}{2d}\left[1 + \frac{2b\epsilon_s}{d\epsilon_m}\right]^{-1},$$
$$L = \mu_0 \frac{2(b + d)}{l_z}, \qquad\qquad \text{Eq. 2-6}$$

where ϵ_m and ϵ_s are the relative permittivities of the metal and spacer, respectively. The current can be found by solving the transmission line equation under the homogenous boundary condition $I(a) = I(-a) = 0$, giving us

$$I(y) = -\frac{H_0 v^2}{k^2}\left(1 - \frac{\cos(ky)}{\cos(ak)}\right). \qquad\qquad \text{Eq. 2-7}$$

Note, the current in the top strip is antiparallel to the current in the bottom strip. Using the current, we can calculate the magnetic moment to be

$$\vec{m} = \frac{1}{2}\int_V \vec{r} \times \vec{j}\, dV \,, \qquad\qquad \text{Eq. 2-8}$$

where the current density is $\vec{j} = j(y)\hat{y} = (I(y)/2bl_z)\hat{y}$, and $\vec{r} \times \vec{j} = j(y)(x\hat{z} - z\hat{x})$. Since the current density is in the x-y plane, the magnetic moment is aligned along the z-axis. Performing the integration of Eq. 2-8 separately along the top and bottom strips, and using the antiparallel nature of the current, we can write the magnetic moment as

$$\vec{m}_z = \frac{1}{2}\int_{V_+} (x\hat{z}) J(y) dV_+ + \frac{1}{2}\int_{V_-} (x\hat{z}) J(y) dV_- , \qquad \textbf{Eq. 2-9}$$

which after integration gives

$$\vec{m}_z = H_0 \frac{al_z(2d + 4b)}{1 - \frac{iZ_m}{\omega L}} \text{sinc}((2d + 4b)k_0)(\text{tanc}(ak) - 1). \qquad \textbf{Eq. 2-10}$$

The z- component of the magnetic susceptibility $\chi_m = nm_z/H_0$ then follows as

$$\chi_m = p \frac{\text{sinc}((2d + 4b)k_0)}{1 - iZ_m/\omega L} \left(\frac{\text{tanc}(ak) - 1}{2}\right), \qquad \textbf{Eq. 2-11}$$

where $n = p/V_R$ is the resonators' number density, p is the resonators surface fraction and $V_R = 4a(d + 2b) l_z$ is the resonator volume.

Figure 2-2 shows the real and imaginary part of the magnetic susceptibility calculated using Eq. 2-11 versus the frequency for three different sizes of the parallel slabs resonators $(a = 39 \, nm, \ a = 85.68 \, nm,$ and $a = 111.39 \, nm)$ and the size of the slab's thickness and spacer's width fixed as $b = d = a/10$.
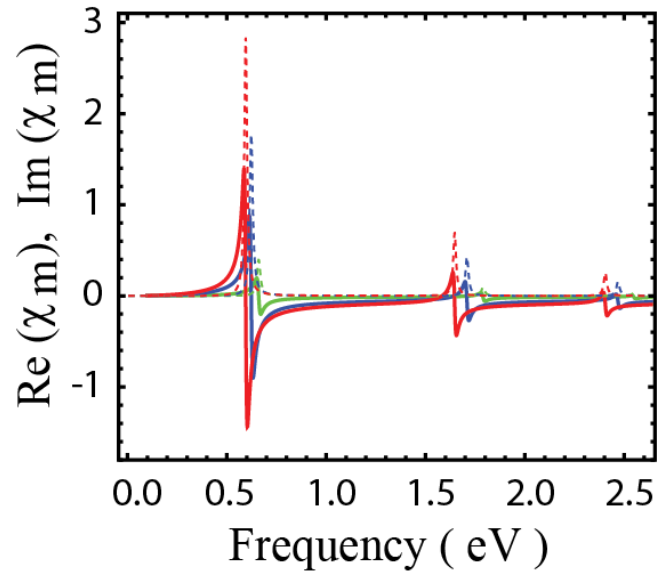
Figure 2-2: The real (solid line) and imaginary (dashed line) parts of the magnetic susceptibility Eq. 2-11 as a function of frequency with considering the lengths of metallic slabs as ($a = 111.4\ nm, a = 85.68\ nm\ and\ a = 39\ nm$) represented by red, blue and green colors, respectively.

Figure 2-2 reveals a strong magnetic response represented by multiple resonances. It is observed that the real part of the magnetic susceptibility reaches negative values for all modes and all three parallel strips' resonators sizes. We also observe that as the size of the resonators decreases, higher magnetic resonance frequency is obtained. The strongest magnetic response of the system is obtained for the first resonance mode ($f = 0.66$ eV) corresponding to a metallic slab's length $a = 111.4\ nm$ represented by red. The higher order resonances appear at higher frequencies and are generally weaker. In the next section, we derive analytical expression for the magnetic frequency resonance which shows explicitly the various size dependencies of the magnetic response.

2.2.2 Magnetic Resonance Frequency

The magnetic susceptibility of parallel slabs metamaterial Eq. 2-11 has a resonant

behavior for a set of frequencies given by the following condition

$$ak = a\omega\sqrt{LC\ (1 - i\ \omega_R/\omega)} = \pi(n + 1/2)\,, \qquad \text{Eq. 2-12}$$

where $(n = 0, 1, 2, ..)$ is the resonance mode number. In Eq. 2-12 the resonator relaxation

frequency is $\omega_R = Z_m/L = -i\eta\ \omega_p^2/\omega^2\epsilon_m$, where η is the geometrical factor and it is

given as $c^2/2b\ (d + b)\omega_p^2$. The permittivity of metallic strips is given by the Drude model

$\epsilon_m = \epsilon_b - \omega_p^2/\omega(\omega - i\omega_\tau)$, where ϵ_b is the contribution due to the lattice electrons, the

plasma and free electrons' relaxation frequencies for silver are $\omega_p = 9.1\ eV$ and $\omega_\tau =$

$0.021\ eV$, respectively. For intermediate frequencies $\omega_\tau \ll \omega \ll \omega_p$ and neglecting losses,

the resonance condition Eq. 2-12 can be written as

$$\omega^2 \frac{(1 + \eta)\widetilde{\omega}_p^2 - \omega^2}{(1 + \eta)\widetilde{\omega}_p^2 - (1 + \eta)\left[1 + \left(\frac{2b\epsilon_s}{d\epsilon_b}\right)\right]\omega^2} = \omega_{n0}^2\,, \qquad \text{Eq. 2-13}$$

where we have introduced the renormalized plasma frequency $\widetilde{\omega}_p^2 = \omega_p^2/\epsilon_b$ and a

characteristic frequency

$$\omega_{n0} = \frac{c\ \pi}{a\sqrt{\epsilon_s(1 + b/d)(1 + \eta)}}\left(n + \frac{1}{2}\right). \qquad \text{Eq. 2-14}$$

To obtain the magnetic resonance frequency, we solve Eq. 2-13 by introducing the

non-dimensional frequency $\nu = \left(\omega/\widetilde{\omega}_p\sqrt{1 + \eta}\right)^2$, then Eq. 2-13 can be written as

$$\nu^2 - (1 + \gamma\Delta_n)\nu + \Delta_n = 0\,, \qquad \text{Eq. 2-15}$$

where $\Delta_n = \left(\omega_{n0}/(\widetilde{\omega}_p\sqrt{1 + \eta})\right)^2$ and $\gamma = (1 + \eta)[1 + (2b\epsilon_s/d\epsilon_b)]$. Finally, we solve

Eq. 2-15 for ν at the resonance condition $\omega = \omega_n$ to obtain

$$\omega_n = \frac{\widetilde{\omega}_p}{\sqrt{2}} \sqrt{(1+\eta)\left(1 + \gamma\Delta_n - \sqrt{(1+\gamma\Delta_n)^2 - 4\Delta_n}\right)} \, . \qquad \textbf{Eq. 2-16}$$

For large resonators $\Delta_n \ll 1$ and $\eta \ll 1$ we have

$$\omega_{n0} = \frac{c\,\pi}{a\sqrt{\epsilon_s(1+b/d)(1+\eta)}}\left(n + \frac{1}{2}\right). \qquad \textbf{Eq. 2-17}$$

For small resonators the resonance frequencies approaches saturation values

$$\omega_{n,s} = \frac{\widetilde{\omega}_p}{\sqrt{1 + \left(1 + \left(\frac{a}{\pi b(2n+1)}\right)^2\right)\left(\frac{2b\epsilon_s}{d\epsilon_b}\right)}} \, . \qquad \textbf{Eq. 2-18}$$

2.2.3 Numerical Simulation Based on the Finite Difference Frequency Domain (FDFD) Method

To check the analytical theory, we have performed full-wave finite difference frequency domain (FDFD) simulations using the COMSOL Multiphysics software. We used the Radio Frequency (RF) model to optimize the magnetic response of the system based on the frequency domain. The numerical model solves the Maxwell's curl equations based on the complex permittivity for two dimensional parallel strips metamaterials placed in vacuum or dielectric material

$$\begin{aligned}\vec{\nabla} \times \left(\vec{\nabla} \times \vec{H}\right) &= \varepsilon_r\,\mu_r\,k_0^2\vec{H} \\ \vec{\nabla} \times \left(\vec{\nabla} \times \vec{E}\right) &= \varepsilon_r\,\mu_r\,k_0^2\vec{E}\end{aligned} \, , \qquad \textbf{Eq. 2-19}$$

where ε_r and μ_r are the complex permittivity and the magnetic permeability of the media.

Once the local electric and magnetic fields are obtained, we apply the polarization current approach to extract the magnetic response of the parallel slabs system. The magnetic moment of the resonator is written as

$$\vec{m}_z(\vec{r}) = \frac{1}{2}\int \vec{r} \times \vec{j}_p dS \, , \qquad \textbf{Eq. 2-20}$$

where the polarization current density is defined as

$$\vec{J}_p(\vec{r}) = i\omega\vec{P}(\vec{r}) = i\omega\epsilon_0(\varepsilon_r(\vec{r}) - 1)\vec{E}(\vec{r}) \,. \qquad \textbf{Eq. 2-21}$$

The effective susceptibility then follows as

$$\chi_m = \frac{nm_z}{H} = \frac{i\omega}{2S_R H} \int \left(\frac{\varepsilon_r(\vec{r}) - 1}{\varepsilon_r(\vec{r})}\right)(xD_y - yD_x)dS \,, \qquad \textbf{Eq. 2-22}$$

where D_y and D_x are the components of the electric field displacement, S is the cross-sectional area of the parallel strips resonators.

The numerically obtained magnetic susceptibility of the parallel strip resonator is shown in Figure 2-3. In the calculations we consider the following parameters, the length of the silver strips is set at $2a = 60$ nm, the thickness is $2b = 3$ nm, and the width of the spacer layer is $2d = 3$ nm.
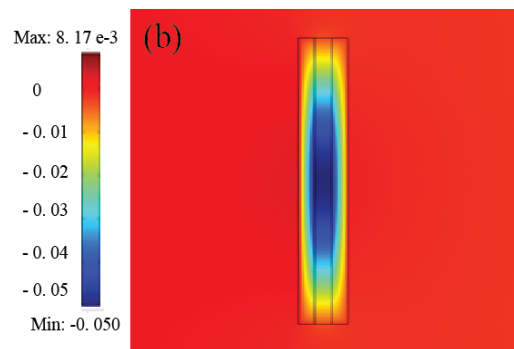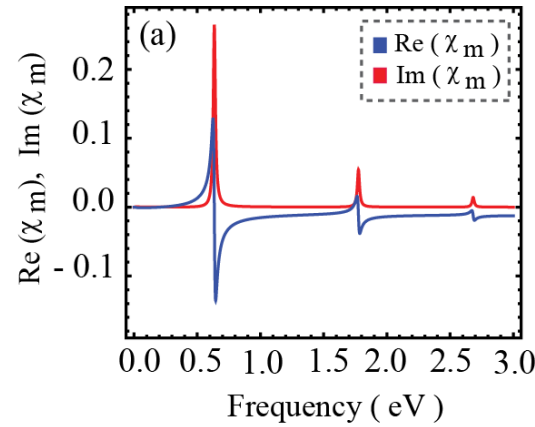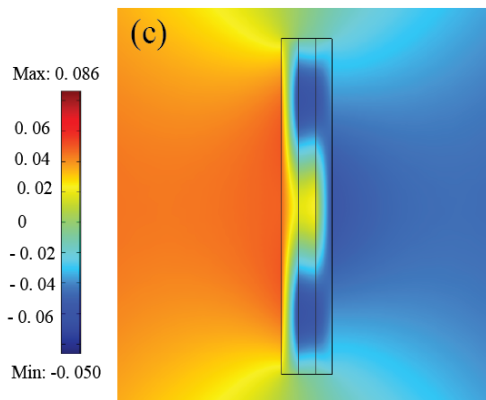
Figure 2-3: Magnetic response of parallel strip resonators: (a) The real and imaginary parts of the magnetic susceptibility in the near and far-infrared spectral range. The dotted line represents the numerical results and the solid line represents the analytical susceptibility. (b) Surface plot of the local magnetic field at the first magnetic resonance frequency (0.636 eV) showing a diamagnetic response (the local magnetic field is antiparallel to the incident). (c) Surface plot of the local magnetic field at the second magnetic resonance frequency (1.776 eV).

Figure 2-3(a) depicts the real and imaginary part of the magnetic susceptibility calculated using Eq. 2-22 versus the frequency. The system shows strong magnetic response represented by multiple resonances within the infrared frequency range. The optimum magnetic response of the system is again obtained for the first mode exhibiting strong diamagnetic response with the real part of the magnetic susceptibility being negative in the frequency ranging from 0.636 eV to 1 eV. Figure 2-3(b) illustrates the local magnetic field profile at the first order resonant frequency $\omega_1 = 0.636$ eV. As expected the magnetic field is localized between the nanostrips and is polarized opposite to the incident magnetic field. The local magnetic field at the second order resonance frequency $\omega_2 = 1.776$ eV is shown in Figure 2-3 (c). Again, strong diamagnetic response is present. In the next section, we show that the magnetic response of the parallel slab system can be tuned by varying the resonator spatial sizes.

2.2.4   Saturation of Magnetic Plasmon Frequency Based on the Scaling of the Parallel Strips Resonators

In Section 2.2.1, we study the magnetic susceptibility as a function of frequency for three different sizes. From Figure 2-2, we observe that decreasing the size of the resonators increases the magnetic resonance frequency. To demonstrate the maximum magnetic resonance frequency that can be achieved using the parallel slabs MMs, we have performed a parametric study of the magnetic resonance frequency as a function of the inverse strip's length 1/a (Figure 2-4) with the corresponding metallic slab's thickness and spacer layer width as b = d= a/10. The numerical values of the magnetic resonance frequency show an excellent match as compared to the analytical result calculated with Eq. 2-16. As we scale down the strips, initially the resonance frequency increases linearly with the inverse strip's length 1/a. This linear relation is applicable only for the low frequency range and can be

estimated using Eq. 2-17. This limiting result is represented with colored dashed lines in Figure 2-4. However, as we further decrease the resonator size, the linear dependence breaks down and for sufficiently small sizes ($a < 100$ nm) a clear saturation is observed. The maximum resonance frequency that can be achieved by this system asymptotically converges to the predicted saturation frequency given by Eq. 2-18. The transmission line theory reveals the physical reason behind the manifested saturation. Specifically, at high frequencies, the metal strips behave as capacitive elements which preclude the excitation of magnetic resonances for frequencies higher than the limiting value $\omega_{n,s} \rightarrow$

$$\tilde{\omega}_p / \sqrt{1 + \left(\frac{2b\epsilon_s}{d\epsilon_b}\right)}.$$
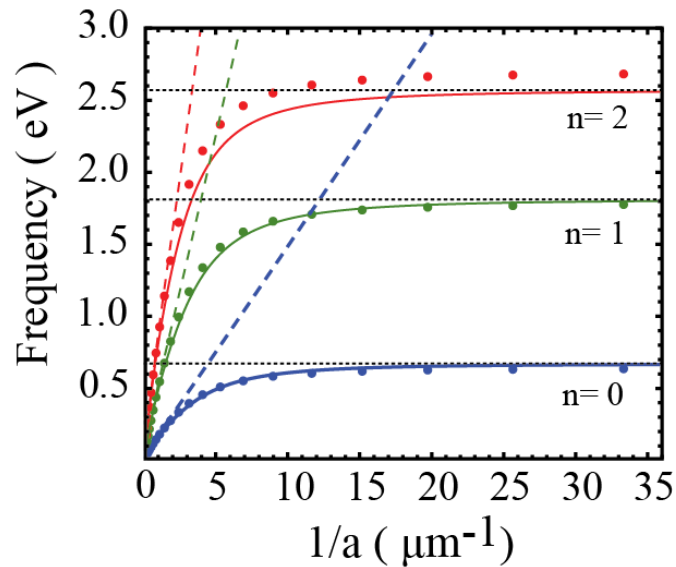
Figure 2-4: Saturation of the magnetic resonance frequency as a function of the inverse resonators length scales. Solid lines represent the analytical theory prediction while and dots represent the numerical results. We consider only the first three modes (starting with blue color to red color). The dashed black lines show the analytically obtained saturation frequency Eq. 2-18 while the dashed (blue, green and red) lines represent the linear response Eq. 2-17 for large size resonators.

2.2.5   Tuning the Magnetic Plasmon Frequency through Varying the Thickness of Metallic Strips

In Figure 2-5, we have optimized the highest possible magnetic plasmon resonance by varying the thickness of the metallic strips for two different lengths, $a = 500$ nm and $a = 800$ nm, with considering $a \gg b$, and the spacer's width is $d = 50$ nm.
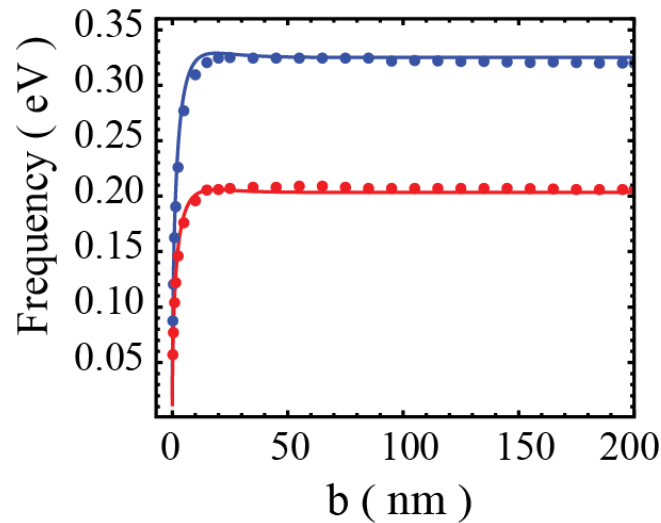
Figure 2-5: Magnetic frequency resonance versus the metallic slab's thickness for two different lengths of the metallic slabs ($a = 500$ nm (blue curve) and $a = 800$ nm (red curve) and the spacer gap $d = 50$ nm. The dots represent the numerical results and the solid lines represent the analytical results given by Eq. 2-18.

From Figure 2-5 we clearly observe that the numerical and analytical magnetic plasmon frequencies calculated using Eq. 2-16 increases by increasing the strip's thickness. The maximum resonance frequency that can be achieved for our structure is $f = 0.325$ eV and corresponds to metallic strip's length $a = 500$ nm. Again, we observe that the magnetic resonant frequency saturates as the thickness of the slab increases beyond the skin depth of $b \geq 20$ nm.

In the next section, we consider more complex geometrical structure (i.e. Bowtie resonators) with the goal of obtaining magnetic response approaching the optical range.

2.3   Bowtie Metamaterials

2.3.1   Analytical Theory of Diamagnetic Response of Bowtie Metamaterials

The system under consideration is composed of silver bowtie structure separated by a dielectric material (i.e. air) in the gap (or spacer) regions. The geometrical parameters of the bowtie structure are a, $4\phi_0$, and $2\pi - 4\phi_0$, where a is the radius of the bowtie, $4\phi_0$ is the azimuthal angle of the gap region, and $2\pi - 4\phi_0$ is the azimuthal angle of the metallic bowtie resonators. The system is illuminated from the top with a harmonic TM-polarized wave with the magnetic field $\vec{H}(\vec{r}, t) = \hat{z}H_0\, e^{-i\vec{k}_0\vec{r}}\, e^{i\omega t}$, where k_0 is the wave vector of light in the free space. To model the magnetic susceptibility χ_m of the bowtie structure depicted in Figure 2-6(a), we solve the Kirchhoff's voltage law for LZ circuit depicted in Figure 2-6(b).
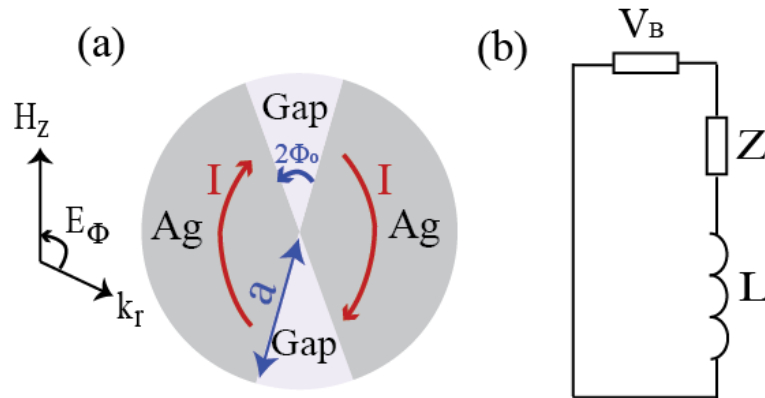
Figure 2-6: (a) Bowtie structure compared to (b) LZ circuit with the source of the magnetic field.

Consider the electromotive source due to the magnetic field in LZ circuit, Kirchhoff's Voltage law can be written as

$$\Delta V_z + \Delta V_L = \Delta V_B,$$
Eq. 2-23

where ΔV_z and ΔV_L are the potential drops due to metal bowtie impedance and inductance, ΔV_B is the electromotive potential given by Faraday's law. Connecting the potential drops to the current, we get

$$Z_{BT} I(t) + L \frac{\partial I(t)}{\partial t} = -\frac{\partial \Phi_B}{\partial t},$$
Eq. 2-24

where the magnetic flux is defined as $\Phi_B = \mu_0 \int \vec{H}(\vec{r}, t).\, d\vec{a}$. Assuming the time harmonic current $I(t) = I(\omega)e^{i\omega t}$, we solve Eq. 2-24

$$I(t) = -\frac{\mu_0 \pi a^2 H(t)}{L} \left(\frac{1}{1 - i \left(\frac{Z_{BT}}{\omega L} \right)} \right),$$
Eq. 2-25

where πa^2 is the surface area of the bowtie structure, Z_{BT} is the total impedance of metallic components and spacer, and L is the inductance. The impedance and the inductance of the bowtie resonators are derived in Appendix A.2 and given as $Z_{BT} = (8\phi_0/i\omega\varepsilon_0\varepsilon_s l_z)(1 + (\varepsilon_s(\pi - 2\phi_0)/2\varepsilon_m\phi_0))$ and $L = \mu_0 \pi a^2/2l_z$, where ε_m is the relative permittivity of silver given by the Drude model (see Section 2.2.2), and ε_s is the relative permittivity of air. The excited asymmetric current, propagates in the $\hat{\phi}$ direction induces a magnetic moment r in the z-direction, hence causing the diamagnetic response of the system. The magnetic moment is then calculated using Eq. 2-8 with current density $\vec{J}_\phi = \hat{\phi} 2rI/l_z a^2$, giving us

$$m_z = -\hat{z}\pi a^2 l_z H_0 \left(\frac{1}{1 - i \left(\frac{Z_{BT}}{\omega L} \right)} \right),$$
Eq. 2-26

where l_z is the depth of the bowtie structure perpendicular to the direction of the resonator place. The magnetic susceptibility χ_m of the bowtie resonator then follows as

$$\chi_m = \frac{nm_z}{H_0} = -\frac{p}{1 - i(Z_{BT}/\omega L)} \; ,$$

Eq. 2-27

where $n = p/V_R$ is the resonators' number density, and $V_R = \pi a^2 l_z$ is the volume of the bowtie structure. Substituting the inductance and impedance, we obtain our final expression

$$\chi_m = \frac{\omega^2}{\omega_0^2 \left(1 + \frac{\varepsilon_s}{\varepsilon_m} \left(\frac{\pi - 2\phi_0}{2\phi_0} \right) \right) - \omega^2} \; ,$$

Eq. 2-28

where we have introduced a characteristic frequency defined as

$$\omega_0 = \frac{4c}{a} \sqrt{\frac{\phi_0}{\varepsilon_s \pi}}$$

Eq. 2-29

The real and imaginary part of the magnetic susceptibility calculated using Eq. 2-28 is illustrated in Figure 2-7. In the calculations, we vary the frequency while the radius of the bowtie resonators is fixed at $a = 10$ nm and the different angles of the dielectric spacer are considered $\phi_0 = 4°$, $\phi_0 = 6°$ and $\phi_0 = 8°$.
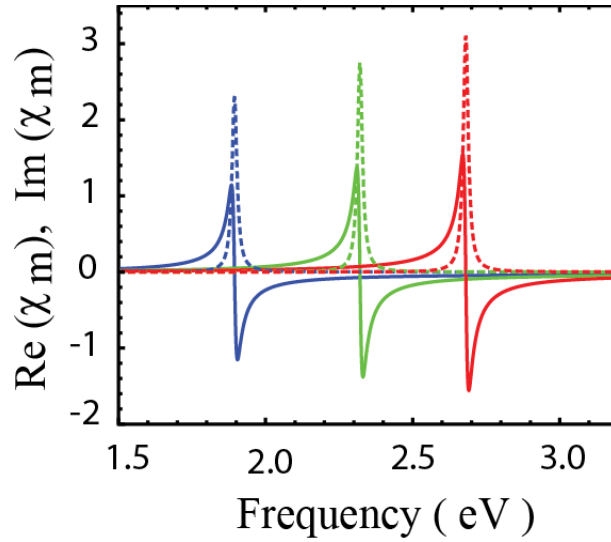
Figure 2-7: Magnetic susceptibility versus frequency. Blue curve is for space angle $\phi_0 = 4°$, green curve is for $\phi_0 = 6°$, and red curve is for $\phi_0 = 8°$. The dashed line represents the imaginary part and the solid line represents the real part.

From Figure 2-7, we observe susceptibility in the frequency ranging between 1.8 eV up to 3.2 eV. The maximum negative magnetic response is obtained for bowtie angle $\phi_0 = 8°$ and at 2.7 eV. In the next section, we derive an explicit relationship for the magnetic resonance frequency.

2.3.2 Magnetic Resonance Frequency

The magnetic susceptibility of the bowtie metamaterial Eq. (2-27) has a resonant behavior when

$$\omega_0^2\left(1 + \frac{\varepsilon_s}{\varepsilon_m}\left(\frac{\pi - 2\phi_0}{2\phi_0}\right)\right) - \omega^2 = 0 . \qquad \textbf{Eq. 2-30}$$

Using the Drude model to describe the metal permittivity, we can write

$$\frac{\varepsilon_s}{\varepsilon_m} = \frac{\varepsilon_s}{\varepsilon_b}\frac{\omega^2\left(\omega^2 - \widetilde{\omega}_p^2\right)}{\left(\widetilde{\omega}_p^2 - \omega^2\right)^2} , \qquad \textbf{Eq. 2-31}$$

and if $\widetilde{\omega}_p^2 = \omega_p^2/\epsilon_b$ is the renormalized plasma frequency, then we can write Eq. 2-30 as

$$(\omega_0^2 - \omega^2)(\widetilde{\omega}_p^2 - \omega^2)^2 + (k-1)\omega_0^2\omega^2(\omega^2 - \widetilde{\omega}_p^2) = 0, \qquad \textbf{Eq. 2-32}$$

where $k - 1 = \varepsilon_s(\pi - 2\phi_0)/(2\phi_0\varepsilon_b)$. Solving Eq. (3-32) for the resonance frequency by assuming the following condition $\nu = \omega^2/\widetilde{\omega}_p^2$ and $\nu_0 = \omega_0^2/\widetilde{\omega}_p^2$, we obtain the characteristic equation

$$\nu^2 - (k\nu_0 + 1)\nu + \nu_0 = 0, \qquad \textbf{Eq. 2-33}$$

and the resonance frequency follows

$$\nu = \frac{1 + k\nu_0 - \sqrt{(1 + k\nu_0)^2 - 4\nu_0}}{2}. \qquad \textbf{Eq. 2-34}$$

Reversing to dimensional units, we arrive at the close form solution

$$\omega_r = \sqrt{\frac{\widetilde{\omega}_p^2 + k\omega_0^2}{2}\left(1 - \sqrt{1 - \left(\frac{2\omega_0\widetilde{\omega}_p}{\widetilde{\omega}_p^2 + k\omega_0^2}\right)^2}\right)}. \qquad \textbf{Eq. 2-35}$$

For small resonators, the resonance frequency saturates at

$$\omega_s \to \frac{\widetilde{\omega}_p}{\sqrt{k}} = \frac{\widetilde{\omega}_p}{\sqrt{1 + \left(\frac{\pi - 2\phi_0}{2\phi_0}\right)\left(\frac{\varepsilon_s}{\epsilon_b}\right)}}. \qquad \textbf{Eq. 2-36}$$

2.3.3   Numerical Simulation Based on Full- Wave Finite Difference Frequency Domain (FDFD)

To check the analytical theory and illustrate the effective magnetic response of the bowtie metamaterials, we have performed numerical simulations using COMSOL Multiphysics software based. The problem we consider is a free standing bowtie resonator placed in the vacuum with scattering boundary conditions applied at the domain boundaries. In the simulations, we consider an incident transfer magnetic (TM) wave propagating in the +z direction. The polarization current approach from Eq. 2-22 is used to extract the magnetic susceptibility.

The numerical results are shown in Figure 2-8 for a bowtie with radius $a = 37.2$ nm and spacer's angle $\phi_0 = 6°$. Figure 2-8(a) presents a real and imaginary parts of the magnetic susceptibility revealing a diamagnetic response within the frequency range from 2.0 eV to 2.3 eV. Figure 2-8(b) shows the local magnetic field profile at the resonance frequency 2.031 eV. The excited local magnetic field is opposite in polarization compared to the incident field demonstrating diamagnetism. The magnetic susceptibility and magnetic plasmon frequency of our structure can be varied by altering the geometrical sizes of the resonators. A comprehensive parametric study of the size dependencies is performed in the next section.
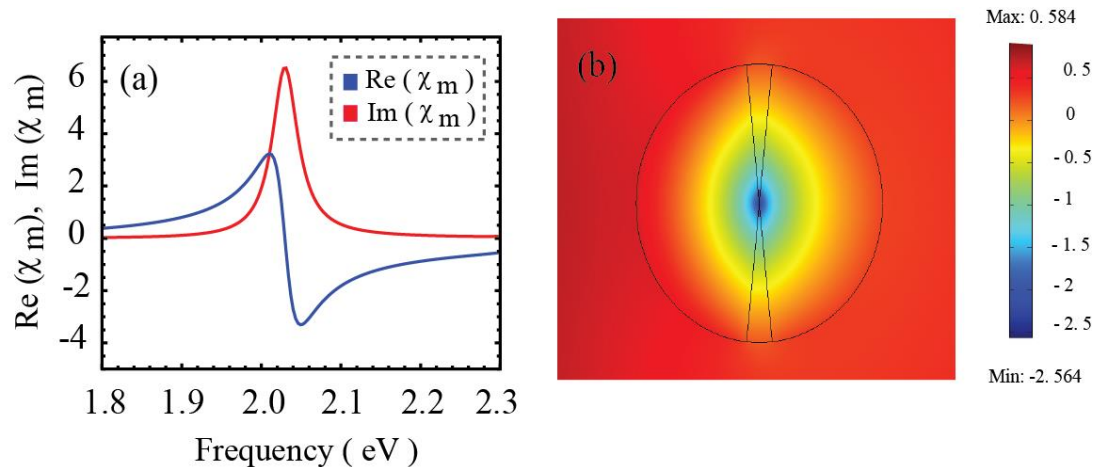
Figure 2-8: Magnetic response of bowtie MMs: (a) The real and imaginary parts of the numerical magnetic susceptibility in the near and far- infrared spectral range. (b) Surface plot of the local magnetic field at the magnetic resonance frequency (2.031 eV).

2.3.4   Saturation of Magnetic Plasmon Frequency Based on the Scaling Structural Sizes of the Bowtie resonators

In Figure 2-9, we show the numerical results for the magnetic plasmon resonance frequency together with the analytical results based on the LZ circuit model Eq. 2-35 versus

the inverse radius $1/a$. These results were obtained by scaling the geometrical sizes of the bowtie resonators for three different dielectric spacer's angle fixed at ($\phi_0 = 4°$, $6°$ and $8°$).
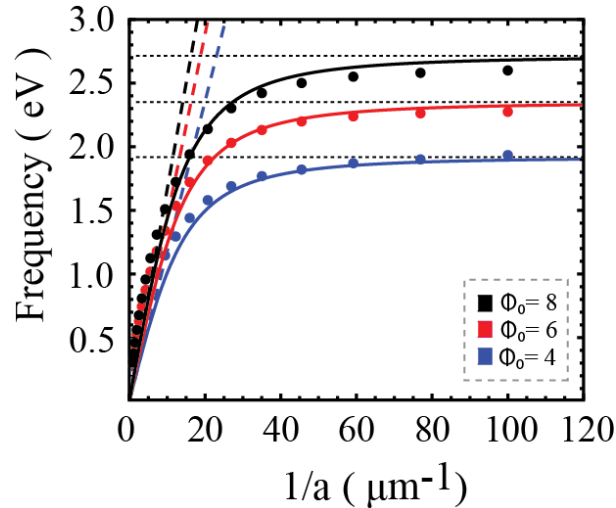
Figure 2-9: Analytical and numerical results for the magnetic resonance frequency as a function of the inverse radius of the bowtie structure for three different angles. The solid lines represent the analytical results and the dots represent the numerical results. The colors corresponds to the bowtie angles $\phi_0 = 4°$ (blue), $\phi_0 = 6°$ (red), and $\phi_0 = 8°$ (black). The dashed black lines represent the analytically obtained saturation frequency.

From Figure 2-9, we observe that for large bowtie resonators, the resonance frequency scales linearly with the inverse resonator's radius. The linear behavior follows closely the analytical result Eq. 2-29 and breaks down as we further decrease the radius of the structure to less than 100 nm. Furthermore, the resonance frequency saturates when the radius of the bowtie reaches very small values, i.e. for $a = 10$ nm.

The saturation frequency calculated analytically using Eq. 2-36 was compared to the numerical resonance frequency represented with (dots) in Figure 2-9, showing good agreement. A maximum saturation frequency of $\omega = 2.6$ eV is obtained for spacer's angle $\phi_0 = 8°$. Clearly, the larger the bowtie angle the higher the magnetic resonance frequency.

In the next section, we provide a comprehensive study of the magnetic frequency resonance

for a fixed radius but changing spacer's angle.

2.3.5 Tuning Magnetic Plasmon Frequency through Varying the Spacer's Angle of Bowtie Resonators

Here, we fix the radius of the bowtie structure at $a = 30$ nm, and study the

magnetic resonance frequency by varying the spacer's angle from $\phi_0 = 0°$ to $\phi_0 = 20°$.

In Figure 2-10, we present both the numerical and analytical results. The resonance

frequency is observed to increase as $\omega_r \approx \omega_p \sqrt{\frac{2\phi_0}{\pi}}$ flowing closely the saturation

frequency Eq. 2-36. The analytical result is nearly identical with that obtained from

COMSOL for angles $\phi_0 < 10°$. For the large bowtie angles, we observe a discrepancy

between the theoretical and numerical resonance frequencies which can be explained by

the fringe effects that are not taken into account in the theory. As a result, at large angles,

the magnetic resonance frequency predicted by the theory saturates at $\widetilde{\omega}_p$ while the actual

saturation value corresponds to the plasmon frequency $\widetilde{\omega}_p / \sqrt{2}$.
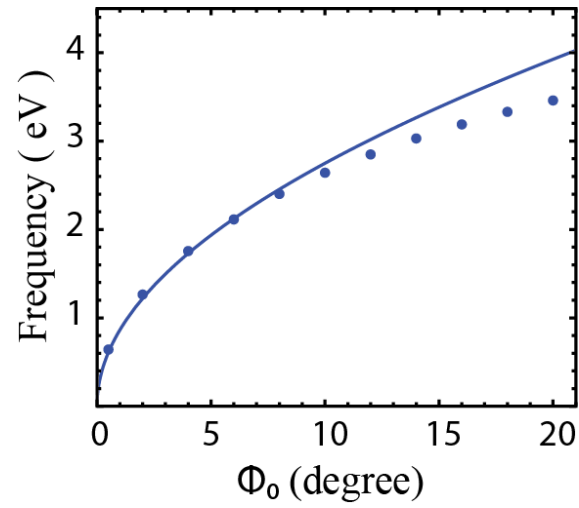
Figure 2-10: The magnetic resonance frequencies obtained numerically (dots) and using the analytical theory (solid lines) versus the dielectric spacer's angle ϕ_0 for a fixed radius $a = 30$ nm.

CHAPTER 3

NEGATIVE INDEX OF REFRACTION IN MMS

3.1   Index of Refraction

The index of refraction is one of the most important optical characteristic of any material and it provides a measure of the speed of an electromagnetic wave as it propagates within a material. In addition, the refractive index also provides a measure of bending a beam of light as it crosses the interface between two different materials. The quantitative measure of this bending is given by Snell's law, $(n_1 \sin \theta_1 = n_2 \sin \theta_2)$, where n_1 and n_2 are the refractive index of the first and second media, respectively, θ_1 and θ_2 are the angles which the light ray makes with the surface normal of each material. For passive medium, the index of refraction is written as $n = n' + in''$, where n' and n'' are the real and imaginary part of the refractive index. In ordinary materials, the refractive index n' is assumed to be positive and the optical refractive indices has a limited value, typically between 1 and 3. However, it was shown by Veselago that a negative refractive index does not violet any fundamental laws of physics [23, 39, 49]. In such materials, Snell's law predicts a rather different behavior of the light rays who will bend to the left of the normal as shown in Figure 3-1, hence left-handed materials.
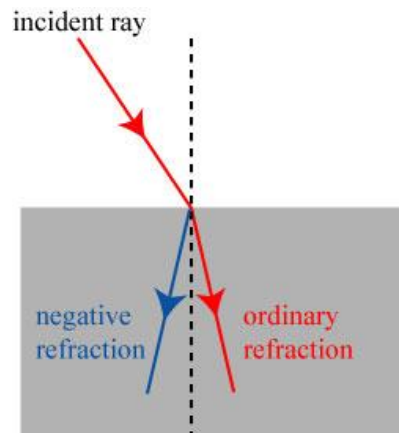
Figure 3-1: Bending of light in ordinary and negative index materials [50].

The refractive index depends on the product of a material's electrical and magnetic responses to an electromagnetic field and is formally written as $n = \pm\sqrt{\varepsilon\mu}$, where ε and μ are the complex permittivity and permeability that are written as $\varepsilon = \varepsilon' + i\varepsilon''$ and $\mu = \mu' + i\mu''$. For ordinary optical materials, both ε' and μ' are positive; therefore, the refraction index is a positive number. However, when ε' and μ' are simultaneously negative, as shown by Veselago, a negative refractive index material is formed [10, 23]. In the presence of losses, a more general condition for negative refraction $\varepsilon''\mu' + \mu''\varepsilon' < 0$ can be derived, and this indicates that $n' < 0$ cannot occur in a passive material which has permeability $\mu = 1 + 0i$ [51]. Therefore, the magnetic response to electromagnetic wave is essential in negative index materials (NIMs). There is no natural material exhibiting a magnetic response at optical frequencies; hence, to demonstrate NIM, it is crucial to engineer and fabricate materials that have strong diamagnetic response at high frequencies. Artificial magnetic response was achieved in metamaterials as discussed in details in Chapter 2. Based on the general condition for achieving negative refraction, we can classify all negative index materials in two types.

1- A double-negative NIM (DN-NIM) is a metamaterial with $\mu' < 0$ and $\varepsilon' < 0$ at the same frequency range.

2- A single-negative NIM (SN-NIM) which has a negative index with either $\mu' < 0$ or $\varepsilon' < 0$ (but not both) [49].

3.1.1   Electromagnetic Responses in Materials

In Chapter 2, we have explained how the magnetic response occurs in a magnetic metamaterial (i.e. SRR structure) and how a negative permeability is obtained as a response to an applied magnetic field through excitation of local currents driven by the electromotive forces. However, it is also important to understand how materials respond to the electric field in order to provide a negative permittivity at a given frequency. In general, materials are classified based on their electric properties as conductors, semiconductors and insulators. For any conductor materials such as noble metals including silver, gold, aluminum and copper, their permittivity is negative below the plasma frequency. Bulk metals are not the only materials that demonstrate negative permittivity. Additional classes of materials are the distributed array of conductors and wires as well as gratings and photonic crystals. Many decades ago, researchers fabricated structures, which show $\varepsilon' < 0$ using arrays of metallic wires and recently various structures were used to provide negative permittivity including cut wire segments, loop wires and straight wires [27, 39]. Additionally, there have been advances in developing electrical MMs to show negative permittivity. The general form for the frequency dependent permittivity of a material is given by the Lorentz-Drude model as

$$\varepsilon_r(\omega) = \varepsilon_\infty - \frac{\omega_p^2}{\omega^2 - \omega_0^2 + i\omega\omega_t}, \qquad \textbf{Eq. 3-1}$$

where ω_p is the plasma frequency $\omega_p = \sqrt{ne^2/\varepsilon_0 m_{eff}}$,where n is the carrier density of electron, e is the electron charge, ε_0 is the permittivity of free space and m_{eff} is the effective electron mass, ω_τ is the damping factor, ω_0 is the resonance frequency, and ε_∞ is the lattice dielectric constant [29].

The Lorentz-Drude model of a material conceptually replaces the atoms and molecules of a real material by a set of harmonically bound electron oscillators, resonant at some frequency ω_0. At frequencies below the resonance frequency, the applied electric field displaces the electrons from the positive core and induces a polarization parallel to the applied electric field. At frequencies near the resonance, the induced polarization becomes very large; however, as the frequency swept through the resonance, the polarization flips from in phase to out of phase with the applied field and the material shows the negative permittivity [41, 29].

For both types of NIMs, the figure of merit (FOM) is commonly used because the low loss NIMs are desired and it is written as

$$FOM = -\frac{n'}{n''} .$$ **Eq. 3-2**

From this definition, we conclude that DN-NIMs is better than SN-NIMs with the same value of the real index of refraction because DN-NIMs have lower imaginary part of the index of refraction than SN-NIMs [10, 49].

In this chapter, we design and simulate NIM by using Comsol Multiphysics software. The electromagnetic properties of the metamaterial are studied using two different approaches which are commonly used to extract the electrical and magnetic responses of composite materials. These two approaches are (a) the local field averaging method and (b) the inverse method.

3.2   Effective Medium Theory: Local Field Averaging Method

Many effective medium theories have been proposed to determine the effective permittivity/ permeability of composite materials such as metamaterials. The most popular and effective medium theories that used mean field approximations to estimate electromagnetic (electrical) properties are Maxwell-Garnett Theory (MGT) and Bruggeman Effective Medium Theory (EMT) [52]. The required condition to apply MGT and EMT is that the size of the inclusions as well as the spacing between the inclusions in the host material must be smaller than the excitation wavelength (quasi-static limit).

Maxwell-Garnet Theory (MGT): The MGT is derived from the Clausius-Mossotti formula, which relates the effective permittivity of the composite to that of the constituent inclusions and the host medium. This implies that higher order multi-pole interactions between the inclusions are not considered; hence, the theory is valid only for small volume fraction of the inclusions usually less than 10% and using higher volume fractions may not provide accurate results [52]

Bruggeman Theory (EMT): This method is widely used homogenization mixing formula to find the effective permittivity of a composite. It considers the polarization effects from nearby inclusions and therefore is valid for higher volume fractions of inclusions compared to MG theory. The maximum concentration of the inclusion can be used for this method is 63%. For higher fraction volume of the inclusions, the system becomes highly complex and may reach the percolation threshold, and therefore there is no analytical model that accurately provides permittivity of the composite medium [53].

Therefore, in this thesis, we solve the composite system numerically by using the COMSOL Multiphysics software. For homogenization purposes, we consider inclusions

with sizes much smaller than the incident wavelength. The numerical approach for homogenization of composite materials with any type of the inclusions is viable and it overcomes the limitations associated with the analytical homogenizations methods. In this section, we introduce the local field averaging method which can be used to estimate the effective magnetic and electrical responses for periodic array of metamaterial structure.

Local Field Averaging Method: If the optical, and geometrical properties of all constituents which make up the composites (i.e. MMs) are known, then to extract the effective optical properties of the composite, we used spatial and ensemble averaging of the local fields within the system. In this method, direct numerical calculations of Maxwell's curl equations are performed

$$\vec{\nabla} \times \vec{E} = -\frac{\partial \vec{B}}{\partial t}, \qquad \vec{\nabla} \times \vec{H} = -\frac{\partial \vec{D}}{\partial t}. \qquad \textbf{Eq. 3-3}$$

The local fields are then used to determine the effective permittivity ε_{eff} and permeability μ_{eff} through the spatial averaging over the unit cell [54], and the effective permittivity and permeability of the system are defined as

$$\langle \vec{D}(\vec{r}) \rangle = \varepsilon_{eff} \langle \vec{E}_0 \rangle, \quad \langle \vec{B}(\vec{r}) \rangle = \mu_{eff} \langle \vec{H}_0 \rangle, \qquad \textbf{Eq. 3-4}$$

where the average electric displacement and magnetic flux density over the unit cell volume V are given as

$$\langle \vec{D}(\vec{r}) \rangle = \frac{1}{V} \int \vec{D}(\vec{r}) dV = \frac{1}{V} \int \varepsilon_r(\vec{r}) \vec{E}(\vec{r}) dV,$$

$$\langle \vec{B}(\vec{r}) \rangle = \frac{1}{V} \int \vec{B}(\vec{r}) dV = \frac{1}{V} \int \mu_r(\vec{r}) \vec{H}(\vec{r}) dV.$$

$$\textbf{Eq. 3-5}$$

For a fixed polarization, we can find the effective permittivity and permeability of the composite as follows

$$\varepsilon_{eff} = \frac{1}{V} \int \frac{\varepsilon_r(\vec{r}) \, E(\vec{r})}{E_0} dV \; , \quad \mu_{eff} = \frac{1}{V} \int \frac{\mu_r(\vec{r}) \, H(\vec{r})}{H_0} dV \; , \qquad \textbf{Eq. 3-6}$$

where E_0 and H_0 are the external electric field and magnetic field, respectively.

Clearly, to be able to use the local field averaging method, first one needs to calculate exactly the local filed profiles, hence the need for the use of numerical codes such as COMSOL Multiphysics. Historically, this method has been utilized to calculate the effective magnetic and electric response of periodic array of parallel microstrips MMs, random metal-dielectric composites and other complex geometries.

3.2.1 Local Field Averaging Method for Periodic Array of Parallel Microstrips Metamaterials

As we mentioned before, the effective optical properties of composite materials can be defined only if the unit cell of the periodic structure is much smaller in size than the incident wavelength of electromagnetic radiation. The proposed MMs is a two-dimensional periodic array of parallel microstrips immersed in a dielectric material. The geometrical outline of the unit cell is schematically shown in Figure 3-2. The length of the microstrips is $2a$, the thickness is b and the gap between the microstrips is d. To extract the effective permittivity and permeability of the system's numerical calculations are performed utilizing Comsol Multiphysics software. The most attractive aspect of metamaterials is that the effective magnetic permeability and permittivity can be controlled by changing the sizes of the unit cell. The majority of designed optical metamaterials rely on metal and dielectric composites to provide effective electric and magnetic responses. However, the MMs can also be designed by invoking highly doped n-type semiconductors, so the magnetic and electric response of metamaterials can be tuned by altering the doping concentration as well.

In this section, we study the magnetic and electric responses for two dimensional metamaterial consisting of silver microstrips immersed in dielectric material (i.e. glass) and these results are compared to similar systems but consisting of n-GaAs microstrips.
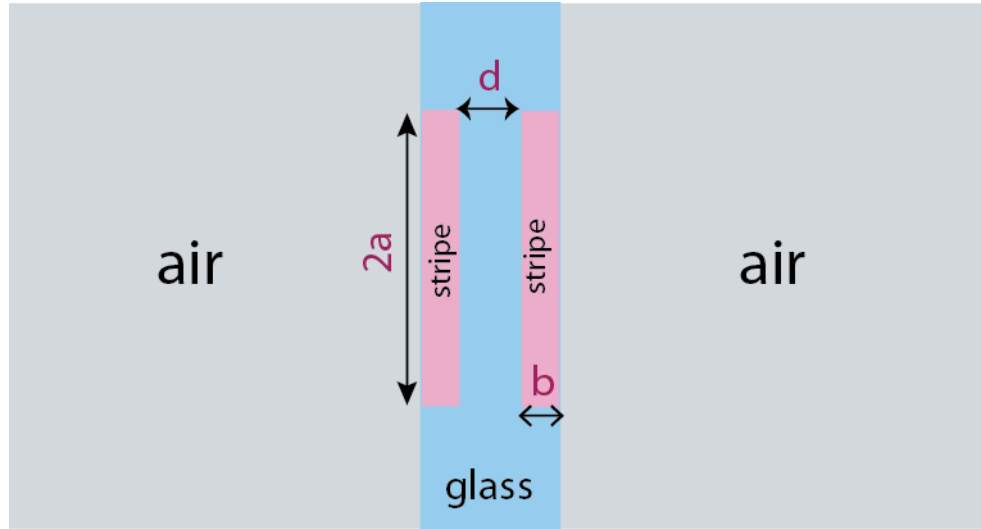
Figure 3-2: Geometrical outlines of the unit cell consisting of two parallel (metallic/ semiconductor) microstrips within a host dielectric material (i.e. glass).

For incident transfer magnetic (TM) wave propagating along the +x axis, the response of the system is calculated using local field averaging method for two-dimensional structure where the magnetic permeability is

$$\mu_e(\omega)H_{z,0} = \frac{1}{S} \int \mu_r(\omega, x, y) H_z(x, y) \, dS, \qquad \textbf{Eq. 3-7}$$

where H_z and H_{z0} are the induced local and incident magnetic fields, respectively, and S is the area of the unit cell. The electric permittivity is calculated similarly as

$$\varepsilon_e(\omega)E_{y,0} = \frac{1}{S} \int \varepsilon_r(\omega, x, y) \, E_y(x, y) dS, \qquad \textbf{Eq. 3-8}$$

where E_y and E_{y0} are the induced local and incident electric fields, respectively.

To demonstrate the effective magnetic and electric properties of the parallel silver microstrips separated by a glass, we fix the thickness and the gap between the strips at $b = 0.35$ μm and $d = 0.8$ μm, and we vary the length of microstrips from $2a = 15$ μm to $2a = 19$ μm. Identically, we attain the magnetic and electric responses of the n-GaAs microstrips separated by a glass for the similar structural sizes and by considering the maximum practical doping concentration $n = 6 \times 10^{25}$ m^{-3}.

The effective permeability for silver and n-GaAs microstrips immersed in a glass are illustrated in Figure 3-3. The negative permeability is observed for both systems; however, the silver resonators show higher resonance frequency compared to the n-GaAs resonators. Although the bandwidth for silver resonators is narrower in comparison to n-GaAs which exhibit a better response to the magnetic field, obtaining negative magnetic response by utilizing n-GaAs provide a material which can be used to fabricate semiconductor devices including THz sensors, transistors, and also it can be used for the applications of negative index materials.
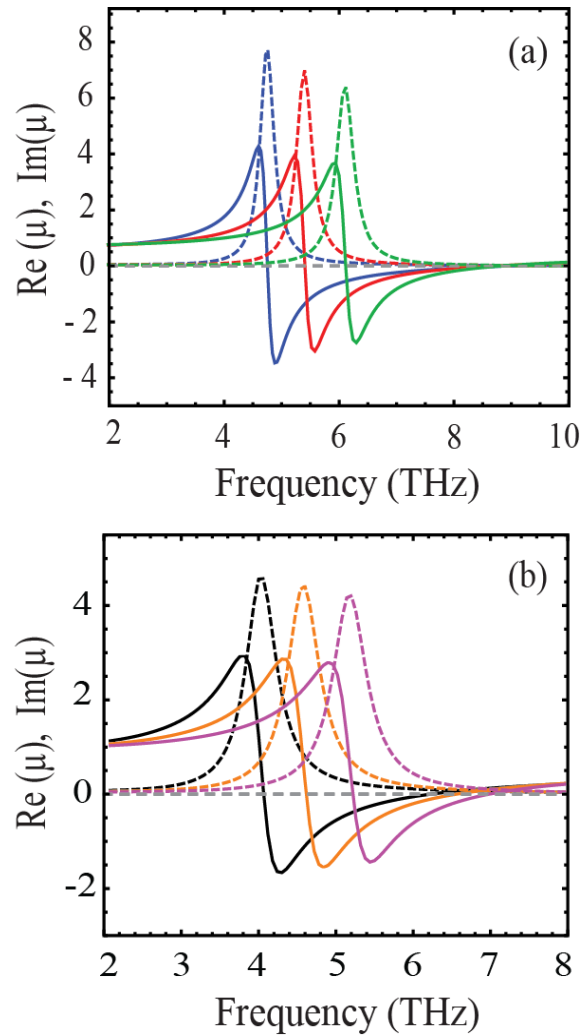
Figure 3-3: Effective permeability versus frequency for three different sizes of the (a) silver and (b) n-GaAs microstrips metamaterial. The real and imaginary parts of the effective permeability are shown with solid and dashed lines, respectively. $2a = 19\ \mu m$ (blue and black), $2a = 17\mu m$ (red and orange), and $2a = 15\ \mu m$ (green and magenta).

Using Eq. 3-8, we have also calculated the effective permittivity of our structure which is shown in Figure 3-4. For the three different lengths of parallel silver microstrips resonators, we observe distinct resonances in the permittivity at low frequencies and asymptotic behavior at large frequencies with $\varepsilon_e \rightarrow 1$ as it should be. A negative real part of permeability is observed only for the larger size resonator ($2a = 19\ \mu m$). Compared to

Figure 3-3, it is clear that using silver strips resonators we can obtain double negative index material within a narrow frequency domain $4.8 \text{ THz} < f < 5.2 \text{ THz}$.

However, for the three different lengths of the parallel (n-GaAs) microstrips resonators under investigation, the effective permittivity is predominantly positive except for $2a = 19 \ \mu m$, the real part of the permeability approaches unity at large frequencies. Despite this deficiency due to the intrinsic loss in the semiconductor, the condition for obtaining a single-negative NIM which has negative index with $\mu' < 0$ but $\varepsilon' > 0$ is still satisfied.
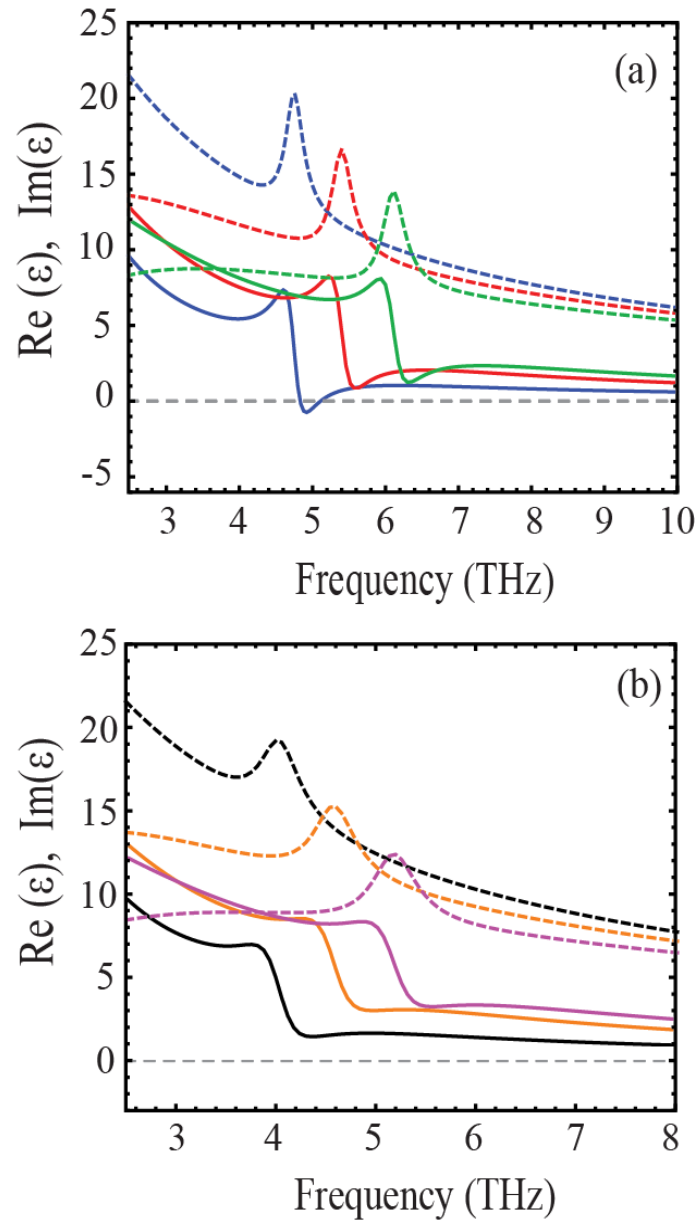
Figure 3-4: Effective permittivity of (a) silver and (b) n-GaAs microstrip resonators as a function of frequency and different microstrips sizes. The colors correspond to the same sizes used in Figure 3-3.

Having obtained both the effective permittivity and permeability of our unit cell,

then we study the effective refractive index presented in Figure 3-5.
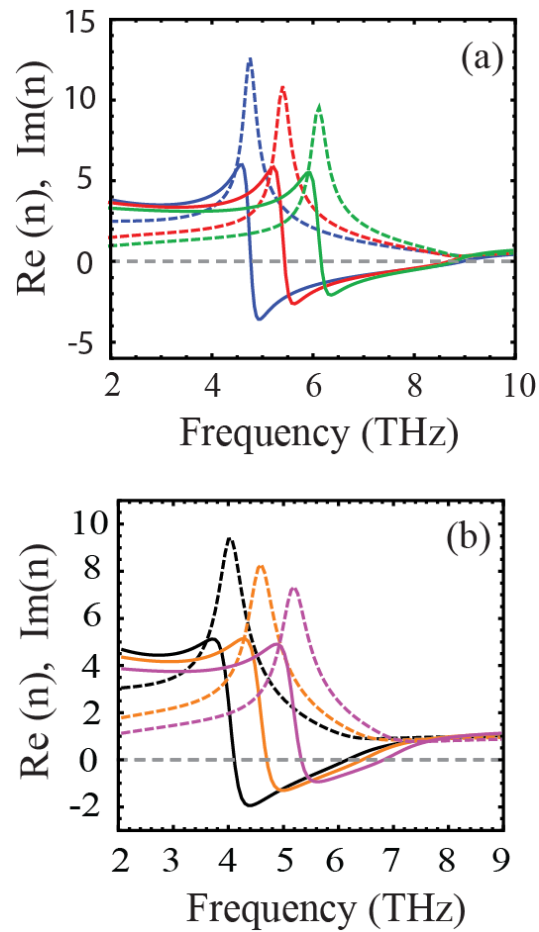
Figure 3-5: Index of refraction as a function of frequency for three different lengths of the microstrips resonators (a) for silver resonators and (b) for n-GaAs resonators. The colors corresponding to the same sizes in which are in Figure 3-3.

We have obtained a negative index of refraction for the investigated sizes of parallel (silver/n-GaAs) microstrips resonators. The highest value of the negative index of refraction is -4.2 at resonance frequency 4.8 THz for silver slabs resonators, while the highest value of semiconductor metamaterials is -2.1 at resonance frequency 4.2 THz. To obtain negative index material at higher frequency, we need to decrease the length of microstrips further; however, to obtain double negative index material, we have to increase the length of the microstrips. To study the performance of negative index material based

on silver and semiconductor, we utilize the figure of merit (FOM) defined in Eq. 3-2. The

highest figure of merit shows the lowest losses in the metamaterial [55]. The FOM as a

function of frequency is depicted in Figure 3-6.
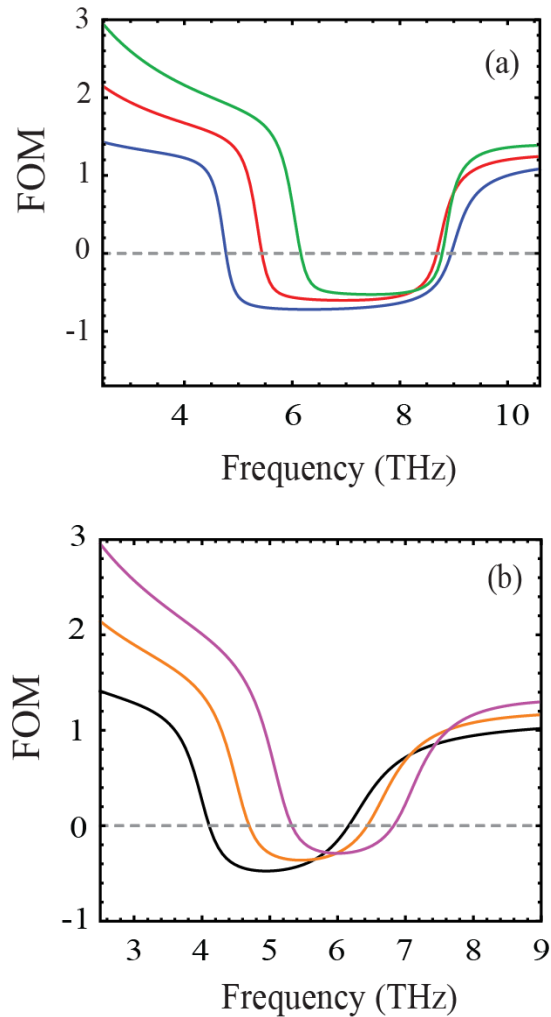
Figure 3-6: Figure of merit as a function of frequency for three different lengths of the microstrips resonators (a) for silver resonators and (b) for n-GaAs resonators. The colors corresponding to the same sizes in which are in Figure 3-3.

In case of silver slab resonators, the maximum FOM of -0.9 is reached within the

frequency range from 5.5 THz to 7.5 THz and that is for double negative index material.

For NIM based on semiconductor, the highest FOM obtained was also for the larger slab's length and the highest value is -0.5 at frequency ranges of 4.5 to 5.4 THz.

To check our results for the field averaging method, we utilized a commonly used method that calculates the optical properties of metamaterials by employing the reflection and transmission coefficients.

3.3   The Inverse Method

The inverse method also known as retrieval method is a second practical approach used to extract the effective electromagnetic properties of metamaterials. This method is based on measuring or simulating the reflection and transmission coefficients for a transverse electromagnetic (TEM) wave normally incidents on the slab of metamaterials. In this procedure, we assume the material to be a homogenous and isotropic with dimensions of the unit cell much smaller than the incident wavelength; hence, the wave in the structure is dominantly characterized by refractive phenomena rather than diffraction or scattering phenomena [56]. Under this condition, the refractive index n and impedance z are obtained by inverting the reflection and transmission coefficients of the metamaterial slab.

Then, we can calculate the effective optical response for a homogenous medium (i.e. metamaterials) represented by electric permittivity ϵ and magnetic permeability μ [56, 57]. In this section, we introduce the extraction method of the material constants for a TEM incident normally on the homogenous slab. In order to obtain the electromagnetic properties of metamaterials, we have also used Comsol Multiphysics software to extract the reflection and transmission coefficients for two types of structures: (1) periodic array of thin slab, (2) parallel slabs of (silver or n-GaAs) immersed in dielectric material.

3.3.1   Inverse Method for a normally Incident TM wave

Consider a transverse magnetic (TM) wave propagating in the x-direction and normally incident as shown in Figure 3-7. Region I and Region III are air and Region II is unknown magneto-dielectric material with thickness d.
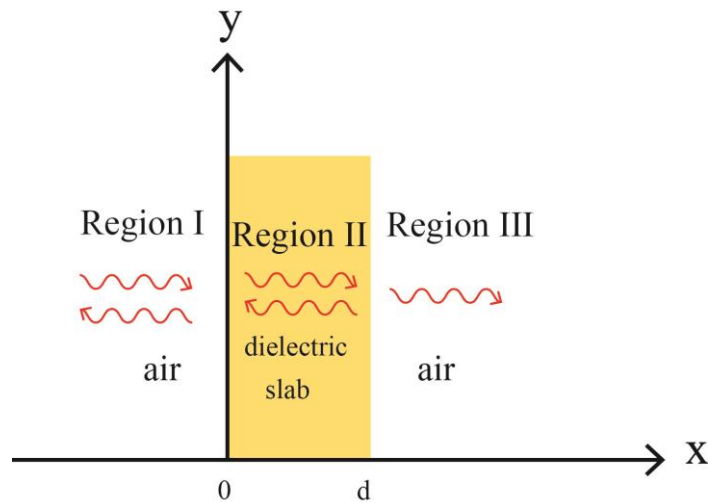
Figure 3-7: Dielectric slab placed in vacuum.

The magnetic field in the three regions can be written as follows

$$
\left.
\begin{aligned}
\vec{H}_1 &= \left(H_1^+ e^{-ikn_1 x} + H_1^- e^{ikn_1 x}\right)\hat{z} \quad &(a)\\
\vec{H}_2 &= \left(H_2^+ e^{-ikn_2 x} + H_2^- e^{ikn_2 x}\right)\hat{z} \quad &(b)\\
\vec{H}_3 &= H_3^+ e^{-ikn_3 x}\hat{z} \quad &(c)
\end{aligned}
\right\} .
\qquad \textbf{Eq. 3-9}
$$

Introducing the reflection, transmission and mixed coefficients $r = H_1^-/H_1^+$, $A = H_2^+/H_1^+$, $B = H_2^-/H_1^+$, $t = H_3^+/H_1^+$, we can recast the magnetic field as

$$
\begin{aligned}
\vec{H}_1 &= \left(e^{-ikn_1 x} + r e^{ikn_1 x}\right)\hat{z}\\
\vec{H}_2 &= \left(A e^{-ikn_2 x} + B e^{ikn_2 x}\right)\hat{z} ,\\
\vec{H}_3 &= t e^{-ikn_3 x}\hat{z}
\end{aligned}
$$

where $n_2 = \pm\sqrt{\epsilon_s \mu_s}$ is the unknown refractive index of the metamaterial slab, and $k = \omega/c$, and these parameters defined as the following r is the reflection coefficients, A and B are constants, t is the reflection coefficients, n_s is the index of refraction of the medium, and k is the wave vector of free space. We can find the electric field in the three regions by using Maxwell's equation for Ampere's law where we should choose the positive sign inside the exponential $+i\omega t$ to be consistent with Comsol software which is used to simulate the electromagnetic responses of MMs. Then the electric field in the three regions is

$$\vec{E}_s = -\frac{1}{i\omega\epsilon_0\epsilon_s}\frac{dH_s(x)}{dx}\hat{y}$$

$$= \pm\,\hat{y}\,z_0 \begin{cases} z_1\left(e^{-ikn_1x} - re^{ikn_1x}\right) \\ z_2\left(Ae^{-ikn_2x} - Be^{ikn_2x}\right), \\ z_3te^{-ikn_3x} \end{cases}$$

Eq. 3-10

where $z_0 = \sqrt{\mu_0/\varepsilon_0}$ is the impedance of free space and we have defined the relative impedance $z_s = n_s/\varepsilon_s$ of the metamaterial slab. Enforcing the continuity of the electric and magnetic fields at the boundaries, we obtain

$$1 - r = \frac{z_2}{z_1}(A - B),$$
$$1 + r = A + B,$$
$$Ae^{-ikn_2d} - Be^{ikn_2d} = \frac{z_3}{z_2}\,te^{-ikn_3\mathrm{d}},$$
$$Ae^{-ikn_2d} + Be^{ikn_2d} = te^{-ikn_3\mathrm{d}}.$$

Eq. 3-11

Solving Eq. 3-11 for the reflection and transmission coefficients, we get

$$r = \frac{(z_1 + z_2)(z_2 - z_3) + e^{2ikn_2\mathrm{d}}(z_1 - z_2)(z_2 + z_3)}{(z_1 - z_2)(z_2 - z_3) + e^{2ikn_2\mathrm{d}}(z_1 + z_2)(z_2 + z_3)},$$
$$t = \frac{4e^{ik(n_2+n_3)\mathrm{d}}z_1z_2}{(z_1 - z_2)(z_2 - z_3) + e^{2ikn_2\mathrm{d}}(z_1 + z_2)(z_2 + z_3)}.$$

In the special case where $n_1 = n_3$ and $z_1 = z_3$, we can simplify the reflection and transmission coefficients as

$$r = -r_{12} \frac{1 - e^{-2ikn_2d}}{1 - r_{12}^2 e^{-2ikn_2d}}$$

$$t = (1 - r_{12}^2) \frac{e^{-ik(n_2-n_3)d}}{1 - r_{12}^2 e^{-2ikn_2d}}$$

Eq. 3-12

where $r_{12} = (z_2 - z_1)/(z_2 + z_1)$. Finally, introducing the normalized transmission coefficient $t' = te^{-idkn_3}$, we obtain the impedance of the slab as follows

$$z = z_2 = \pm \sqrt{\frac{(1 - r)^2 - t'^2}{(1 + r)^2 - t'^2}}$$

Eq. 3-13

Furthermore, from Eq. 3-12, we obtain the following relationships

$$\frac{1}{t'} = \cos(n_2 kd) + \frac{i}{2}\left(z + \frac{1}{z}\right)\sin(n_2 kd)$$

$$\frac{r}{t'} = -\frac{i}{2}\left(z - \frac{1}{z}\right)\sin(n_2 kd).$$

Substituting $\sin(n_2 kd)$ from the second equation in the first we obtain

$$\cos(n_2 kd) = \frac{1}{t'}\left[1 + r\left(\frac{z^2 + 1}{z^2 - 1}\right)\right] = \frac{1 - r^2 + t'^2}{2t'}.$$

Using $\cos(dkn_2) = \cos(\pm dkn_2) = \cos(\pm(dkn_2 - 2\pi m))$, we can invert to obtain the index of refraction of the dielectric slab as

$$n_2 = \pm\frac{1}{kd}\cos^{-1}\left(\frac{1 - r^2 + t'^2}{2t'}\right) + \frac{2\pi m}{kd}, \quad \mathrm{Im}(n_2) > 0, \qquad \text{**Eq. 3-14**}$$

where m is an integer number. In the extraction procedure, the sign choice is fixed independently by enforcing the conditions $\mathrm{Re}(z) > 0$ and $\mathrm{Im}(n_2) > 0$. A major issue in the extraction method is selecting a correct sign for $\mathrm{Re}(n_2)$ and a proper branch cut given

by the integer number m. Finally, using Eq. 3-13 and Eq. 3-14 we can find the permittivity and permeability of the slab as

$$\varepsilon = n/z, \quad \mu = zn .$$ **Eq. 3-15**

3.3.2 Extraction of Material Constants of a Homogeneous Slab Using Full Wave Calculations

To demonstrate the validity of the retrieval method, we first study a unit cell of a slab of material placed in vacuum. Figure 3-8 reveals the simulation scheme for extracting of the reflection and transmission coefficients for a transverse magnetic (TM) wave that impinges 2-dimensional slab with given constant permittivity and permeability. Using the extracted reflection and transmission coefficients, we calculate the permittivity and permeability of the slab using the inverse method. When performing the calculations, a periodic boundary conditions are applied to the upper and bottom phases of the simulation domain. The incident p-polarized magnetic wave enters the simulation domain at $x = x_0$ and exits at $x = x_L$. The length and the width of the slab are L and d, respectively.
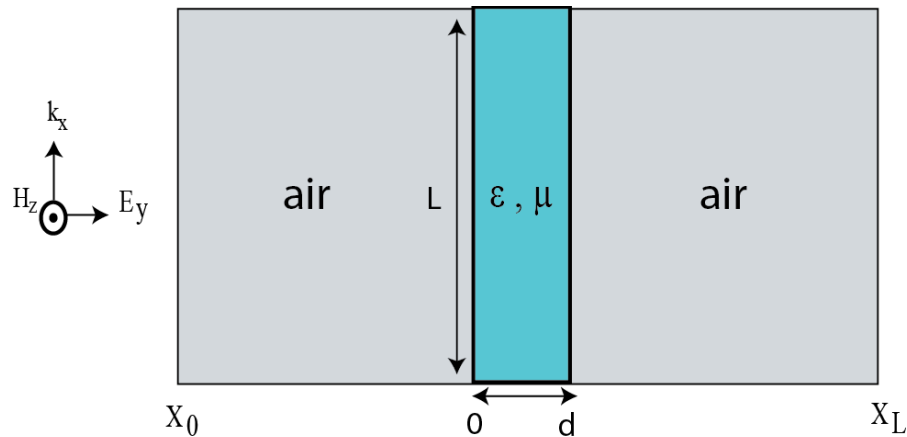
Figure 3-8: Simulation domain for extracting the reflection and transmission coefficients of a slab of given material placed in vacuum.

The reflection and transmission coefficients can be calculated numerically by integrating the local magnetic field at the front and back sides of the simulation domain using the following equations

$$r = \frac{1}{L}\int H_z(x_0, y)\left(e^{-ik_x x_0} - e^{-2ik_x x_0}\right) dy ,$$

$$t = \frac{1}{L}\int H_z(x_0, y)e^{ik_x x_L} dy .$$

Eq. 3-16

The numerically obtained transmission and reflection coefficients are then used to extract the impedance and the index of refraction (Eq. 3-13 and 3-14) of the slab as well as the effective permittivity and permeability utilizing Eq. 3-15.

We apply this inverse method for three types of structures: a medium consists of a nondispersive slab, a medium composed of a dispersive slab, and a medium comprised of periodic array parallel microstrips immersed in a host material.

3.3.2.1 Inverse Method - non-dispersive slab of material

Here, we consider a rectangular slab of nondispersive medium where the index of refraction is fixed and independent of frequency. The width and the length of the slab are fixed at $d = 1.5\ \mu m$ and $L = 20\ \mu m$ and the permittivity and permeability of the slab are set at $\varepsilon = 3$ and $\mu = 1$. The numerically obtained reflection and transmission coefficients are shown in Figure 3-9 and found to be consistent with the analytical results using Eq. 3.12. This validates the extraction formulas Eq. 3-16 which will be used extensively below.
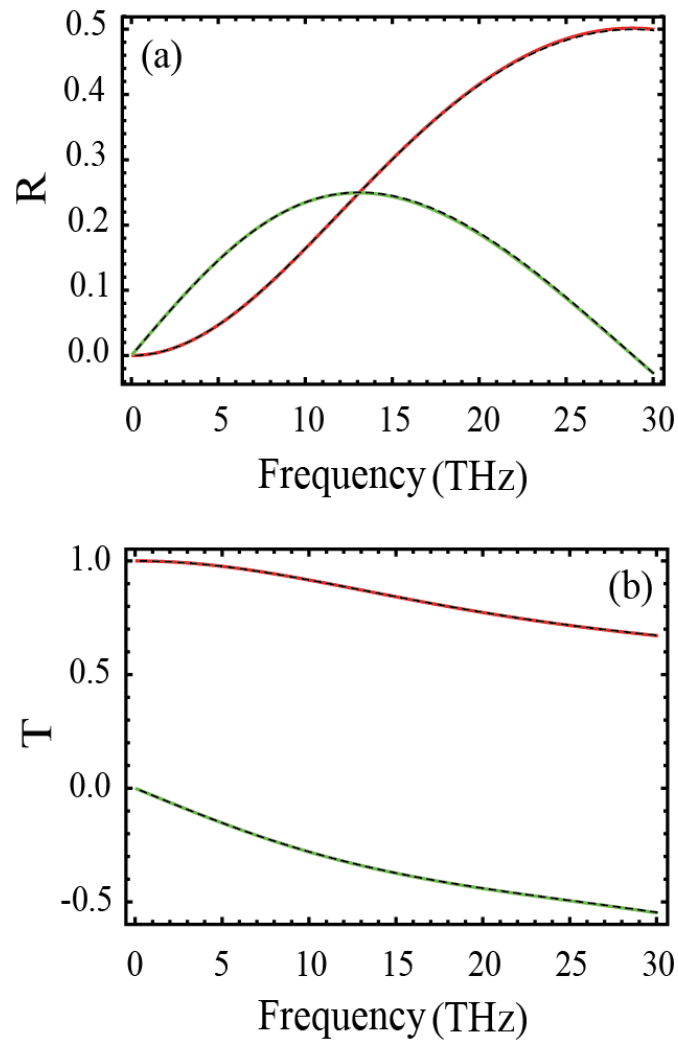
Figure 3-9: Reflection and transmission coefficients versus frequency. The real part (red) and imaginary part (green) of (a) the reflection coefficients and (b) transmission coefficients for nondispersive medium are calculated using Comsol software and are compared the analytical results (dashed lines).

The recovered impedance Eq. 3-13 and index of refraction Eq. 3-14 were calculated based on the simulated data of the extracted transmission and reflection coeffcients are shown in Figure 3-10.
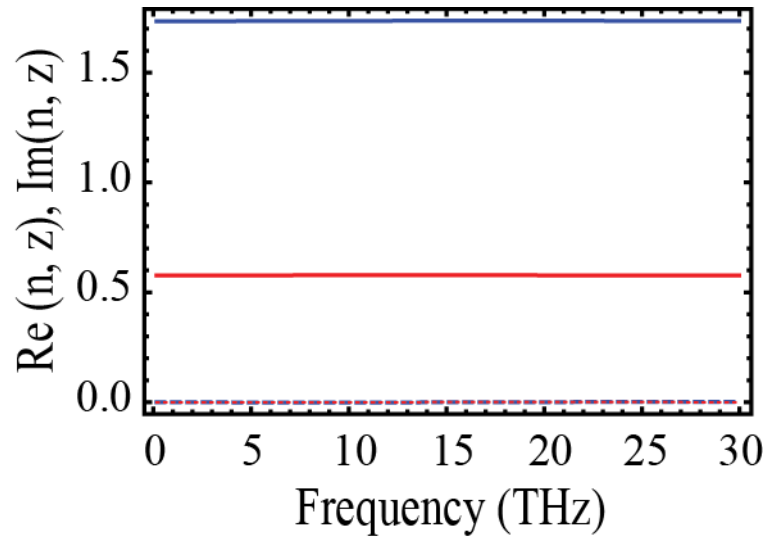
Figure 3-10: Extracted index of refraction (blue color) and impedance (red color) as a function of frequency. Solid lines represent the real parts and dashed lines are the imaginary parts.

As we can observe from the figure, the retrieved refractive index and impedenace are independent of frequency, as they should. The real part of the index of refraction (solid blue line) and the real part of the impedance were in good agreement with the theoretical results calculated respectively as $n = \sqrt{\varepsilon\mu} = 1.73$ and $z = \sqrt{\mu}/\sqrt{\varepsilon} = 0.577$. The imaginary part for the index of refraction and impedance is zero as expected and they are shown with dashed lines in Figure 3-10. Finally, we calculate the permittivity and permeability of nondispersive slab using Eq. 3-15 based on the numerical index of refraction and impedance. The obtained results are demonstrated in Figure 3-11 where the green color represnts the retrieved permittivity and the permeability is shown by the magenta color.
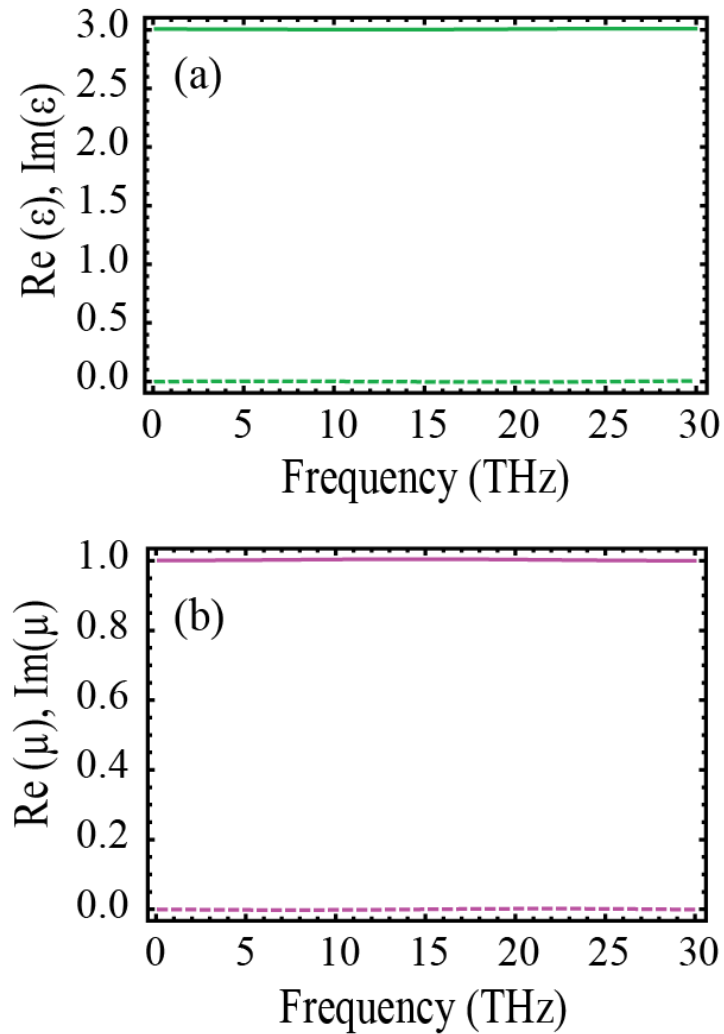
Figure 3-11: Retrieved permittivity (a) and permeability (b) versus frequency. The real and imaginary parts are represented with solid and dashed lines, respectively.

We notice from Figure 3-11 that the recovered permittivity and permeability of the nondispersive medium calculated utilizing the simulated reflection and transmission coefficients exactly match to the input permittivity and permeability, which verifies the retrieval procedure. In the next section, we consider a slab of dispersive material.

3.3.2.2 Inverse Method - dispersive slab of material

Here, we consider a slab of a dispersive material. In this case, the inverse method is used to retrieve the material constants of a Lorentz dielectric material where the permittivity of the slab is frequency dependent and given by Eq. 3-1 while the permeability is unity. In this example, we set the parameters of the Lorentz's material as plasma frequency $f_p = 10$ THz, relaxation frequency $f_t = 2$ THz, and resonance frequency $f_0 = 6$ THz. The Comsol Multiphysics software is used again to extract the reflection and transmission coefficients shown in Figure 3-12.
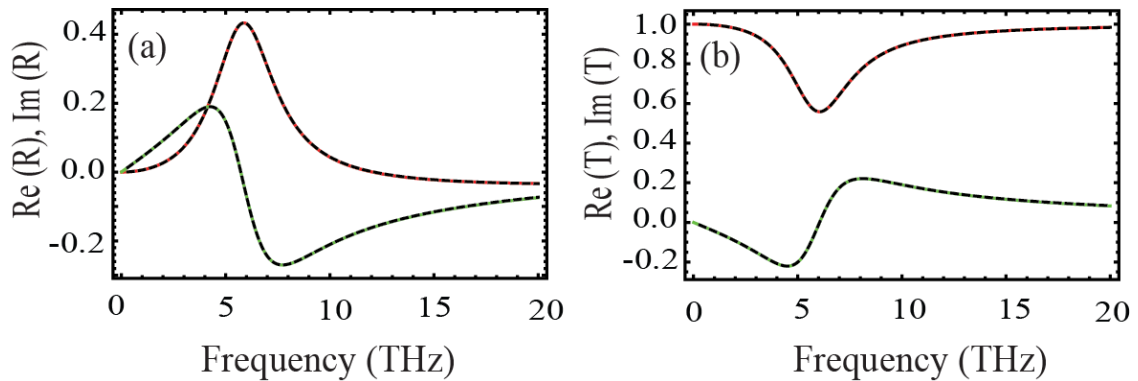
Figure 3-12: Calculated real (red color) and imaginary (green color) parts of (a) reflection coefficients and (b) transmission coefficients as a function of frequency for slab of dispersive material. The solid lines correspond to the numerical simulations while the dashed curves are the analytical results.

From Figure 3-12, we recognize that again the theoretical results were in good match with the simulated reflection and transmission coefficients for the dispersive medium. Hence, we next proceed to calculate the impedance and index of refraction (Eq. 3-15) using the numerically obtained reflection and transmission coefficients and compare our results with the slab's actual impedance and index of refraction. The results for the

impedance and index of refraction versus frequency are shown in Figure 3-13 and in Figure 3-14, respectively.
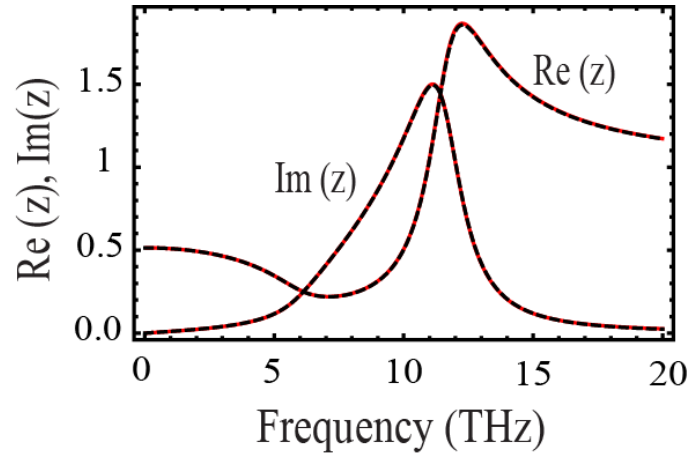
Figure 3-13: Real and imaginary parts of impedance as a function of frequency for a dispersive slab. The theoretical results are represented with dashed line while the numerical results are represented with the red color.
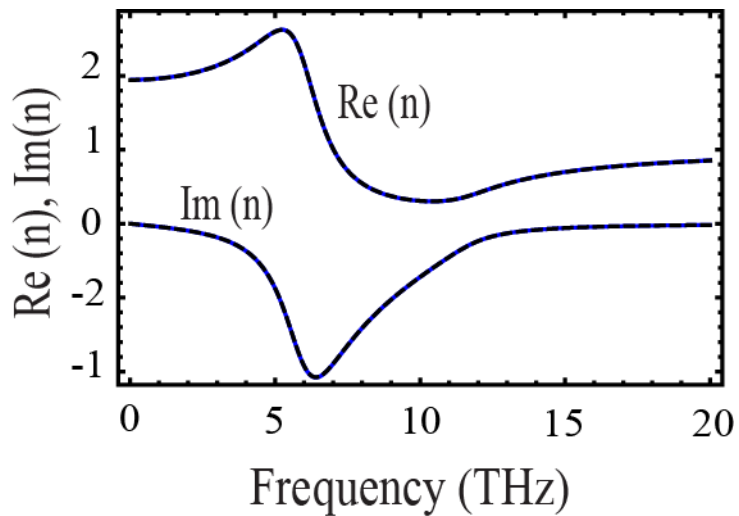
Figure 3-14: Real and imaginary parts of the refractive index as a function of frequency for a dispersive slab. The theoretical results are represented with dashed line while the numerical results are represented with the blue color.

We observe from Figure 3-13 and Figure 3-14 that the extracted impedance and index of refraction are in excellent agreement with the pre-set values, again validating the inverse method. Finally, we proceed with the extraction of the permittivity and permeability of the slab using Eq. 3-15. The extracted data is compared to the pre-set permittivity given by the Lorentz's model in Figure 3.15.
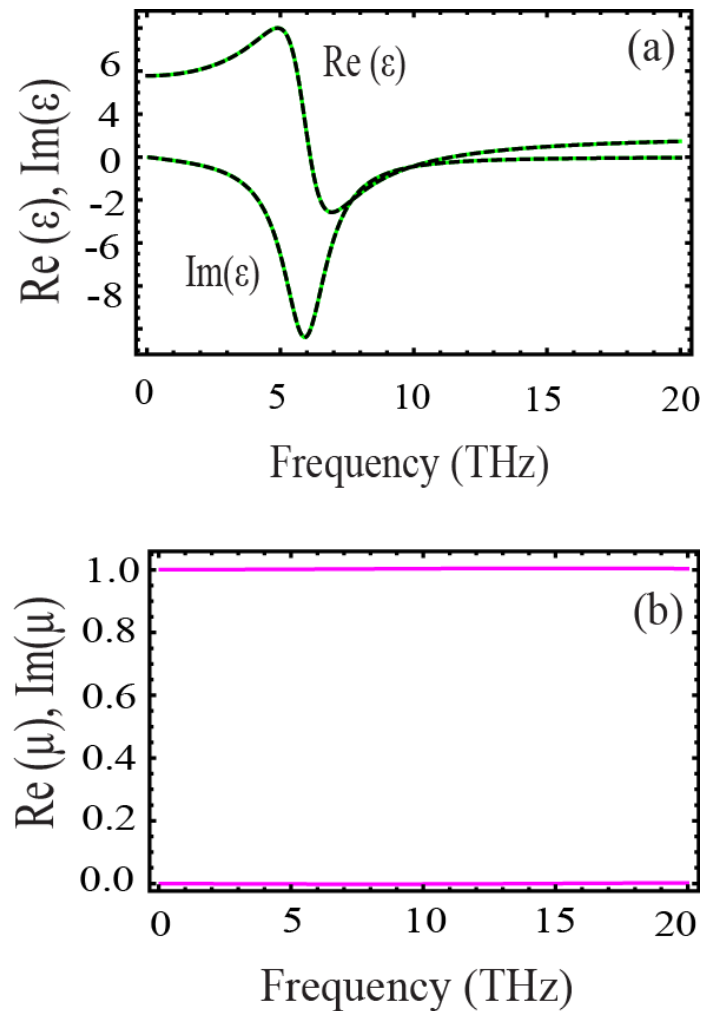
Figure 3-15: Plot of the real and imaginary part of permittivity (a) and permeability (b) versus the frequency.

The numerically retrieved permittivity and permeability are shown to be consistent with the pre-set Lorentz model and unit permeability. The performed investigations of the inverse method have thus verified its accuracy and indicates that this method is well applicable for the extraction of the electromagnetic responses of slab materials described by homogeneous, isotropic and dispersive electric permittivity and permeability. Therefore, we proceed by applying the inverse method to more complicated, inhomogeneous parallel slabs' metamaterial structures.

3.3.2.3 Inverse Method – parallel microstrip metamaterials

Here, we consider a periodic array of metamaterial where the unit cell consists of two-dimensional parallel microstrips immersed in a dielectric host material. The geometrical properties of the structure under consideration are similar to the metamaterials studied with the field averaging method (see Figure 3-2, Section 3.2.1). The goal of this investigation is to extract the permittivity and permeability of the parallel slabs (using silver and n-GaAs) metamaterial using inverse method and compare these results to those based on the local field averaging. Such comparison between the methods will provide a pathway for designing metamaterial structures. We follow the same procedure of the inverse method by considering the identical structural sizes for the glass, which is considered as a host material and the parallel microstrips immersed in the glass. The thickness of the considered microstrip is fixed as well as the size of the glass slab, however the length of the microstrips are varied as $2a = 15\ \mu m, 2a = 17\ \mu m, 2a = 19\ \mu m$. The extracted impedance for Ag-glass system and n-GaAs-glass system is demonstrated in Figure 3-16.
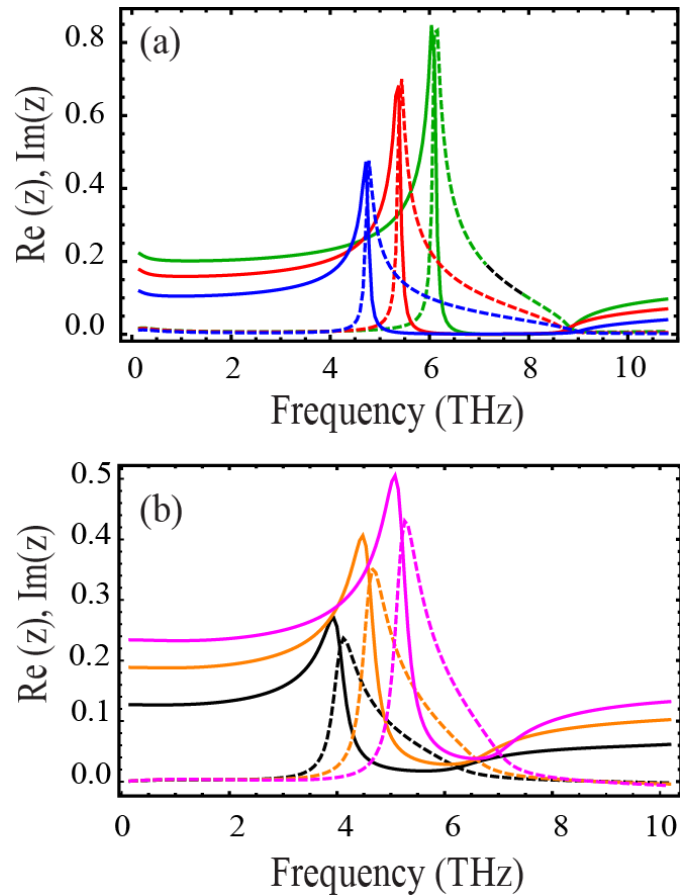
Figure 3-16: Real and imaginary part of the impedance of (a) silver on glass and (b) n-GaAs on glass microstrip resonators versus the frequency. The solid lines corresponding to the real part while the dashed lines represent the imaginary part. In the calculations we consider three resonator sizes $2a = 19 \ \mu m$ (blue and black lines), $2a = 17 \ \mu m$ (red and orange lines), and $2a = 15 \ \mu m$ (green and magenta lines).

We notice from Figure 3-16 that by decreasing the size of the resonators, we obtain higher impedance for both resonator systems (silver-glass, and n-GaAs-glass). Additionally, the silver-glass system shows higher resonance frequency for the considered length of the resonators and for $2a = 15 \ \mu m$, there is a discontinuity for the imaginary part of impedance in the frequency range between 7.1 to 7.9 THz. To resolve this problem, we

have selected the negative solution for imaginary part of the impedance Eq. 3-13. The extracted index of refraction for both systems is shown in Figure 3.17.
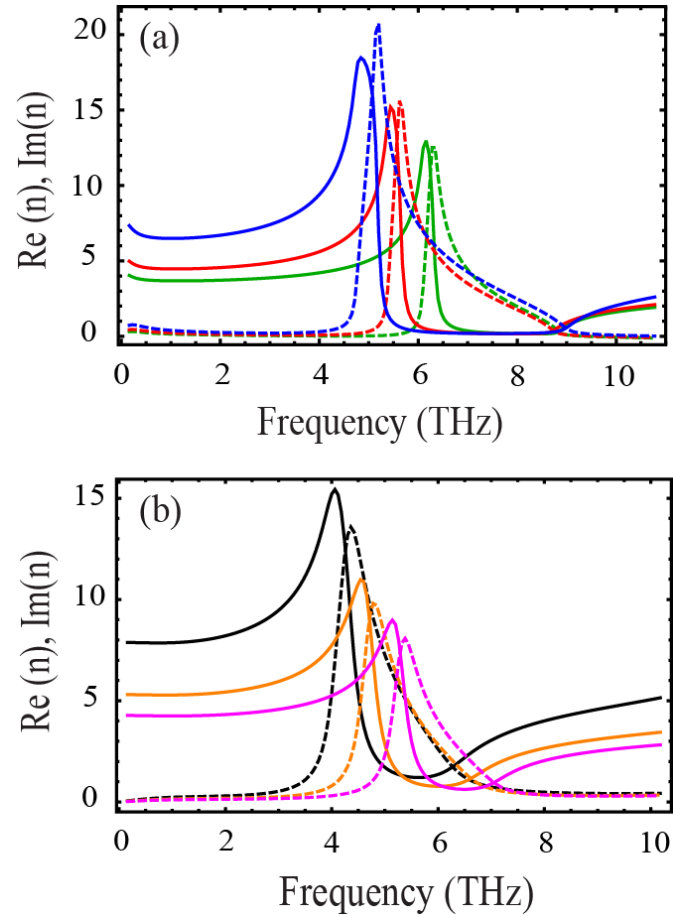
Figure 3-17: Index of refraction as a function of frequency for (a) silver on glass and (b) n-GaAs on glass microstrip resonators. The solid lines corresponding to the real part while the dashed lines represent the imaginary part. In the calculations, we consider three resonator sizes $2a = 19\ \mu m$ (blue and black lines), $2a = 17\ \mu m$ (red and orange lines), and $2a = 15\ \mu m$ (green and magenta lines).

Figure 3-17 shows that the real part of the index of refraction decreases as the length of (silver/ n-GaAs) decreases and the maximum resonance frequency obtained is 6.6 THz for the silver-glass system which exhibits zero index of refraction. Therefore, from this demonstration, we can conclude that for obtaining negative index material used, we have

to further decrease the microstrips' length and for realizing the low losses for negative index materials, the n-GaAs is the preferred material for the microstrips. Finally, using the extracted index of refraction and impedance, we retrieve the magnetic permeability and electric permittivity and the results are depicted in Figure 3-18 and Figure 3-19, correspondingly.
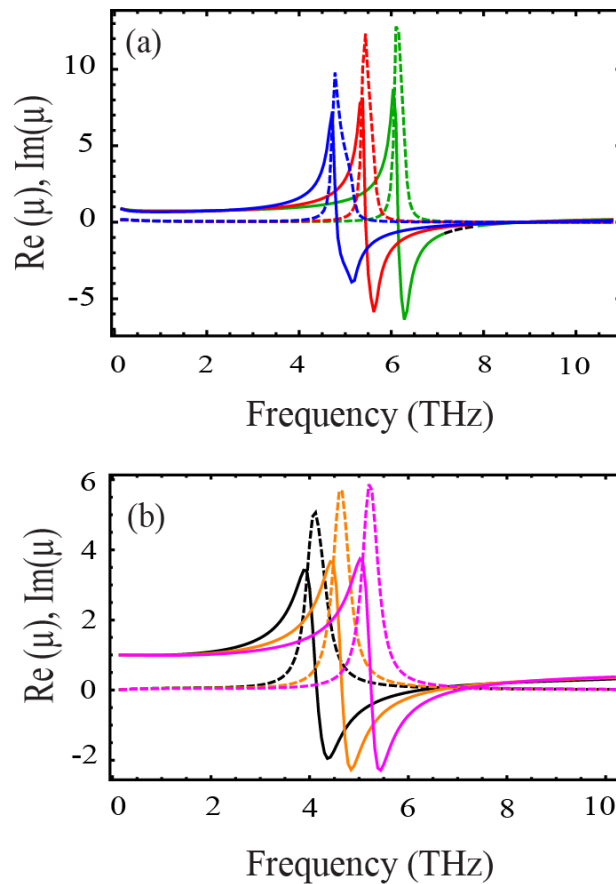
Figure 3-18: Real and imaginary part of magnetic permeability for (a) silver on glass (b) n-GaAs on glass microstrip resonators versus the frequency. The solid lines corresponding to the real part while the dashed lines represent the imaginary part. In the calculations we consider three resonator sizes $2a = 19\ \mu m$ (blue and black lines), $2a = 17\ \mu m$ (red and orange lines), and $2a = 15\ \mu m$ (green and magenta lines).

We observe from Figure 3-18 that the magnetic permeability decreases as we scale down the length of the microstrips, and it shows the maximum negative permeability at higher frequencies. For the n-GaAs on glass resonators, the maximum negative permeability is -2.3 at frequency equals to 5.4 THz, and the length of the resonators is $2a = 15\ \mu m$.
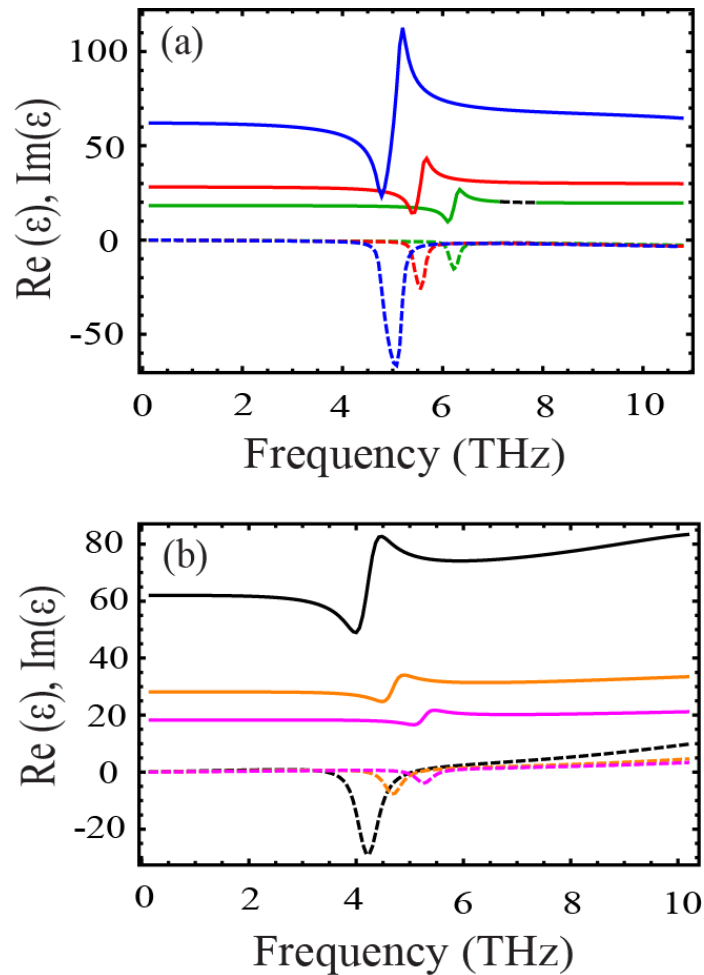
Figure 3-19: Real and imaginary part of electric permittivity for (a) silver on glass (b) n-GaAs on glass microstrip resonators versus the frequency. The solid lines corresponding to the real part while the dashed lines represent the imaginary part. In the calculations we consider three resonator sizes $2a = 19\ \mu m$ (blue and black lines), $2a = 17\ \mu m$ (red and orange lines), and $2a = 15\ \mu m$ (green and magenta lines).

Figure 3-19 illustrates the parallel microstrips permittivity, showing distinct electrical resonances for all sizes of the resonators. We notice that the retrieved permeability and permittivity show a discontinuity region for microstrips of length $2a = 15\ \mu m$ in frequencies ranging between 7.1 to 7.9 THz. In this region, a second branch cut must be chosen.

Comparing the local field averaging method with the inverse method, we notice that all resonance frequencies pertaining to the index of refraction agrees well between the methods. The magnetic resonance frequencies also match in both methods; however, we observe opposite behaviors. For the field averaging method, as the length of the resonators decreases, we notice a decrease in the strength of the magnetic response. However, the inverse shows that decreasing the length of microstrips increases the magnetic response. Additionally, the extracted permittivity by the inverse method demonstrates opposite behavior as compared to the field averaging method.

To summarize, our results show that both extraction methods predict identical magnetic susceptibilities, but under resonance conditions they can deviate when extracting the electric response of the system. This should serve as a point of caution for the community since both methods are widely used in the literature with little or no attention paid to possible inconsistencies.

CHAPTER 4

NO$_X$ SENSOR

4.1   Introduction to NO$_x$ Sensors

Diesel engines produce much higher particulates and NO$_x$ exhaust gas compared to gasoline engines. NO$_x$ is used to represent nitric oxide (NO) and nitrogen dioxide (NO$_2$), which can cause many health problems, as well as smog and acid rain. In order to reduce and limit the emission of NO$_x$ gases as required by many governments, NO$_x$ gas sensors were developed for automotive and trucking applications [58, 59].

The US Environmental Protection Agency (EPA) has proposed regulations which require NO$_x$ sensors to monitor NO$_x$ in diesel vehicles [60, 61]. In order for NO$_x$ sensors to remain effective, it is necessary to improve the sensitivity, selectivity, stability, response time, and accuracy [58].

NO$_x$ sensors are a type of electrochemical cell consisting of electrolyte and electrode. Platinum is typically used as the electrode material in NO$_x$ sensors. As for the electrolyte material, conventional NO$_x$ sensors are based on a zirconia ZrO$_2$ electrolyte due to its high conductivity, which promotes NO$_x$ sensitivity. In addition, ZrO$_2$ compatible at elevated tailpipe temperatures of 400℃ and above. Furthermore, ZrO$_2$ is chemically stable in both reducing and oxidizing atmospheres [59, 62]. Conventional NO$_x$ sensors consist of a dense electrolyte and porous electrodes. Porous electrodes allow gas diffusion to the triple

phase boundary (TPB) where the gas, electrode and electrolyte come into contact, thereby enabling charge transfer (i.e. reduction or oxidation) reactions effecting sensitivity to NO_x. Even though porous electrodes support diffusing the gases, they can also reduce the concentration of NO_x at TPBs, since they enable heterogeneous catalysis. This negatively impacts sensor accuracy [58]. To address this problem, dense electrodes have been proposed. Many studies reveal that sensors with the dense electrode were less prone to heterogeneous catalysis and more sensitive to NO [63, 64]. This new sensor design incorporates porous electrolytes to enable gas diffusion to TPBs. Highly porous electrolytes can promote a rapid sensing response, yet the high porosity results in fewer sites for NO_x reactions, thereby limiting NO_x sensitivity. On the other hand, electrolytes of limited porosity have resulted in high NO_x sensitivity, but are accompanied with a slow sensing response. The slow response is due to limited gas diffusion rates. Thus, a practical sensor must have a microstructure that strikes a balance between promoting gas diffusion and ionic transport through the electrolyte bulk [58].

Impedancemetric gas sensors promise more accurate NO_x detection at the single ppm level. In this method, an alternating voltage is applied at a specific frequency resulting in an electrical response. Then, the impedance is calculated as a ratio of signal voltage over the current. The resulting AC impedance phase angle can be used to measure the NO_x response with a very high stability, accuracy, and sensitivity, in comparison to the conventional amperometric gas sensing method. Given the benefits of this approach impedancemetric NO_x sensors were evaluated was used in this work [58, 60].

Studying the porosity of the sensor electrolyte is very important, as the electrolyte microstructure affects the impedancemetric NO_x sensing response. Such a study will help

the development of NO_x sensors as optimization of the microstructure and morphology can improve sensor performance. The Archimedes method is one means for obtaining measurements of the electrolyte porosity. Coupling this method with scanning electron microscopy will enable the electrolyte porosity to be evaluated with respect to the electrolyte morphology (i.e., particle size, tortuosity, and particle connectivity).

In this chapter, experimental work is presented for fabricating yttria stabilized zirconia (YSZ) electrolyte pellets and varying the porosity by fabricating the pellets at temperatures ranging from 1050℃ -1350℃. YSZ was selected as the electrolyte material as the yttria doping contributes to the ionic conductivity of the electrolyte, which promotes sensitivity to NO_x.

4.2 Experimental Work

4.2.1 Fabrication of YSZ Electrolyte Pellets

Yttria stabilized zirconia (YSZ) pellets were fabricated by making a slurry consisting of 8 mol % Y_2O_3- ZrO_2 powder, polyvinyl butyral binder, and ethanol. Then the slurry was ball milled over night to get homogenous mixture. The slurry was dried on the hot plate, then ground using a mortar and pestle. After the grinding process, the processed powder was pressed at 200 MPa into pellets with the diameter of 1 cm. The pellets were fired at temperatures of 1050-1350℃ for 1 hour. Scanning electron microscopy was used to observe the morphology and microstructure, while Archimedes measurements were performed to determine the porosity. An impedance spectroscopy was carried out to evaluate the electrical response and sensing characteristics.

4.2.2 Archimedes Measurement

The porosity of the pellet is theoretically calculated as

$$\phi = \left(\frac{V_p}{V_b}\right) \times 100\% = \frac{V_b - V_m}{V_b} \times 100\% \,, \qquad\qquad \textbf{Eq. 4-1}$$

where V_b is the bulk volume of the pellet, V_m is the matrix volume, and V_p is the pore volume. However, we measured the porosity of our sample (i.e. pellet) experimentally by using Archimedes method [65], which, based on the weight of the pellets, and it is defined as

$$\phi = \frac{V_b - V_m}{V_b} = \frac{W_{sat} - W_{dry}}{W_{sat} - W_{sub}} \,, \qquad\qquad \textbf{Eq. 4-2}$$

where the bulk volume and matrix volume expressed in terms of weight of the dry, saturated and submerge YSZ pellet as $V_b = (W_{sat} - W_{sub})/\rho_{fluid}$ and $V_m = (W_{dry} - W_{sub})/\rho_{fluid}$, where ρ_{fluid} is the density of fluid, W_{sat} is the weight of the saturated pellet, W_{dry} is the weight of the dry pellet and W_{sub} is the weight of submerge pellet. The measurement was done three times for each sample, and then the average porosity and the standard deviation were calculated in Table 4-1. The plot of the average porosity as a function of temperature is shown in Figure 4-1.

Table 4-1: Measuring the average porosity for YSZ electrolytes at various firing temperatures.

T (ºC)	Ave Porosity %	Standard deviation of the measurement
1050	43.73	0.058
1100	42.7	0.14
1150	37.72	0.032
1200	35.9	0.97
1250	22.64	0.056
1300	9.44	0.15
1350	3.35	0.099
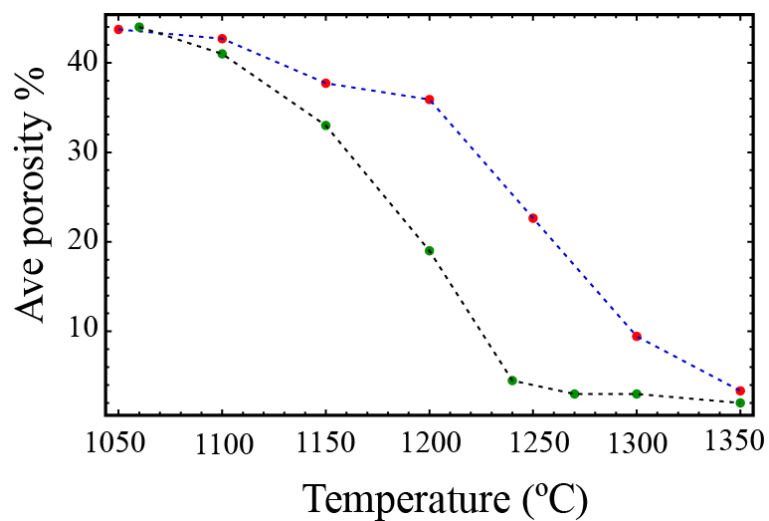
Figure 4-1: Plot of the average porosity as a function of the temperature (red dots) compared to the average porosity of the other study given in ref [66].

In Figure 4-1, the average porosity calculated using Archimedes measurement for YSZ pellets by varying the temperature (see Table 4-1). The red dots show experimental data, and the green dots are comparison data from another study [66]. We can observe from Figure 4-1 that the porosity decreases by increasing the temperature, which comparable with the average porosity calculated in [66] at low firing temperature. However, as the firing temperature exceeded 1150℃, we can see a clear discrepancy between our data and the data measured in ref [66]. This discrepancy is related to the firing time of YSZ electrolyte where in the other study, the firing time of YSZ electrolyte was longer (i.e., 2 hours) which made the electrolyte to be denser and the pore size to be smaller in comparison to our data for YSZ pellets fired for one hour.

4.2.3 Scanning Electron Microscopy (SEM)

SEM Images of YSZ electrolyte pellets fired at 1050ºC, 1100ºC, 1150ºC, 1200ºC, 1250ºC, 1300ºC, and 1350ºC are shown in Figure 4-2. We can notice from the images that the particle sizes and pore structure alters with changes in the firing temperature. At lower temperatures, the pore size was 43.73%, and as the temperature increased, the pore size decreased and the particle coalesced at 1350ºC. The connectivity between the particles increased with firing temperature. For YSZ pellets fired at 1350ºC, the structure became denser and few open pores remained as indicated by the low porosity of 3.35% as determined by Archimedes method.

The goal of this study is to fabricate sensors containing a porous electrolyte and dense electrode. In the following section, fabrication of porous NO_x sensors is discussed.
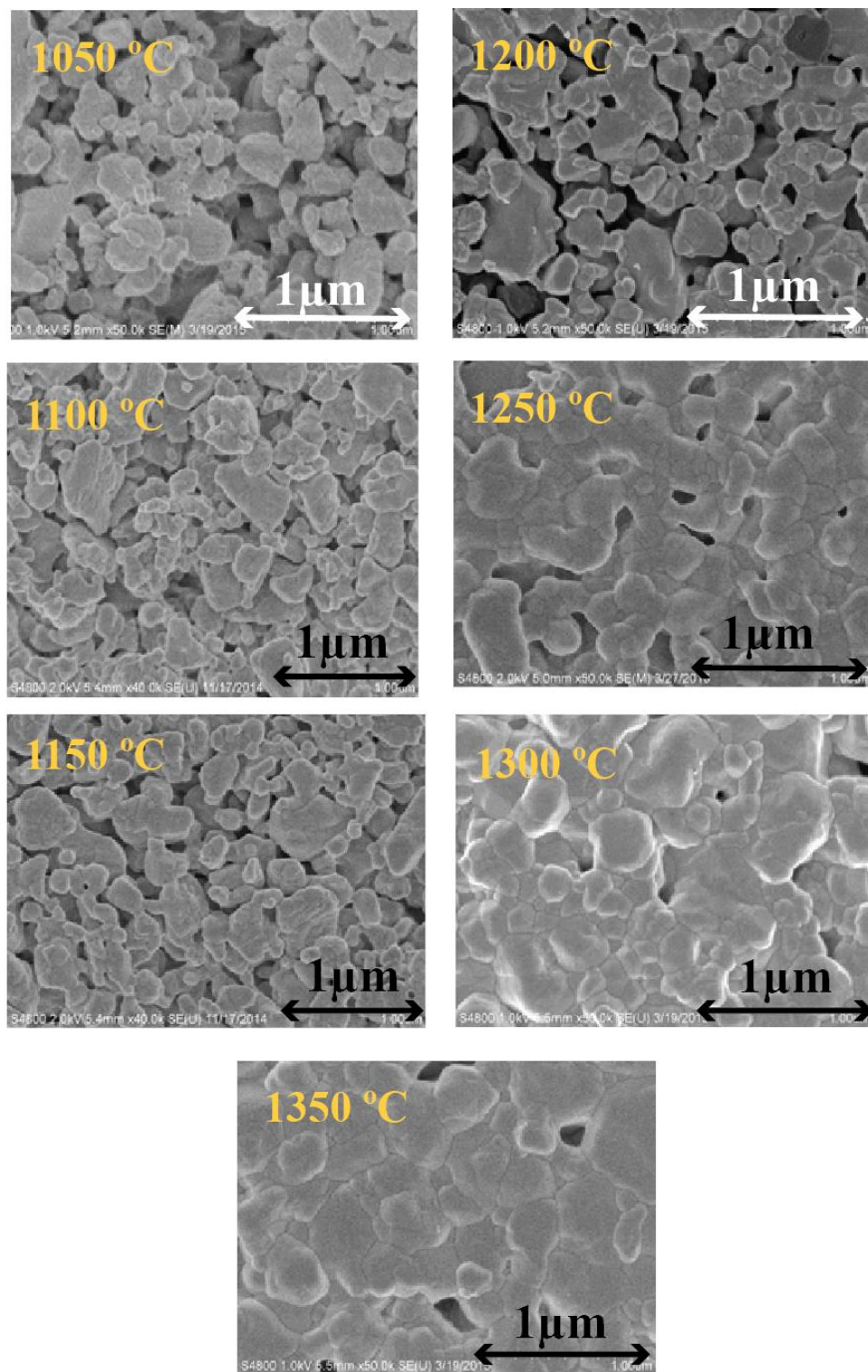
Figure 4-2: SEM images for the YSZ pellets fired at varying temperature from T = 1050℃ to T = 1350℃.

4.3   Fabrication of NO_x Sensor

The YSZ pellets were fabricated into NO_x sensors by attaching symmetric gold (Au) wires to serve as the counter and sensing electrodes. The gold wire were 0.2 mm in diameter and the distance d between the gold wires was 0.5 cm as shown in Figure 4-3(a). YSZ slurry remaining from the process described in Section 4.2.1 was applied over the Au wires in order to embed the electrodes within the sensor electrolyte. Several coats of the slurry were applied to sufficiently embed the electrodes. The coating process is shown in Figure 4-3(b). The sensors were allowed to dry at room temperature while the slurry coating was applied. This step was repeated until the final structure of NO_x sensor was formed, see Figure 4-3(c). In Figure 4-3(c), the gold wires were also coated in order to protect them during firing. Au melts at approximately $1060^{o}C$. The coating enables the Au to remain intact during firing at $T > 1050^{o}C$. This coating was removed from the Au wires after firing in order to connect the sensor to the impedance analyzer for electrochemical evaluation.
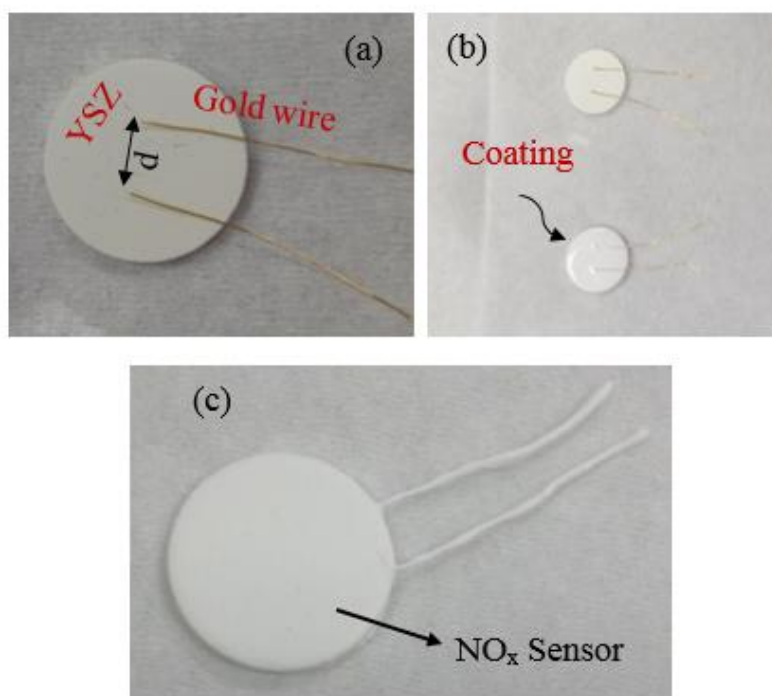
Figure 4-3: Fabrication of NO_x sensor. (a) The YSZ electrolyte with the parallel gold wire where d is the distance between the wires, (b) image of YSZ coating and the attached gold wires and (c) The final NO_x sensor with embedded gold wires.

4.3.1   Electrochemical Impedance Spectroscopy (EIS)

The sensors were loaded into a quartz tube and placed in a furnace for analysis by electrochemical impedance spectroscopy (EIS). The gold wire electrodes from the sensor were connected to a Gamry Reference 600. A standard gas handling system was used to introduce dry mixtures of N_2, O_2, NO and NO_2. The experiments were performed 0-100 ppm NO and NO_2 at a flow rate of 100 sccm (standard cubic centimeters per minute) with O_2 concentrations ranging from (1-18%). The measurements were collected at operating temperatures of 600-700℃. Impedance measurement were collected for a frequency range between 1 MHz to 1 Hz at ten steps per decade where the excitation amplitude was 50 mV. The goal of this work was to observe how impedance response under various operating

conditions was impacted by the different electrolyte microstructures. Moreover, the sensor microstructure on sensor sensitivity and selectivity would contribute to understanding of the feasibility of the NO_x sensor design.

4.3.2   Results of Electrochemical Impedance Spectroscopy (EIS)

Presented here are the results of NO_x sensors operated using the impedancemetric method. The Nyquist plots demonstrate the impedance response for various conditions.

4.3.2.1 Nyquist Plot

Typical Nyquist plots of the impedance spectrum for two sensors fired at 1050℃ and 1100℃ are shown in Figure 4-4 and Figure 4-5, respectively, in the presence of 10.5% with N_2 as the balance. In both figures, the impedance measurement varied based on changing the operating temperature ranging from 600℃ to 700℃. These were taken without presence of the NO gas. In the Nyquist plot, two arcs were present. The large arc to the right represented the low frequency region, while the smaller arc to the left represented the high frequency region. The low frequency region described the mass transfer or interfacial processes. The diameter of the arc represents the resistance associated with the process. The impedance arcs decreased as the temperature increased and these arcs became smaller as the YSZ porosity decreased. Similar behavior occurred for sensors fired at 1100℃, and the results are shown in Figure 4-5.
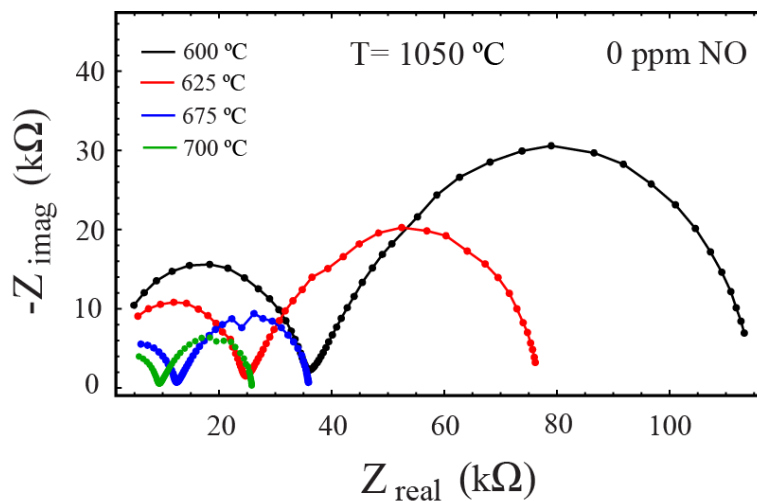
Figure 4-4: Nyquist plot of NO_x sensor fired at 1050℃ without NO and by varying the temperature from 600℃ to 700℃.
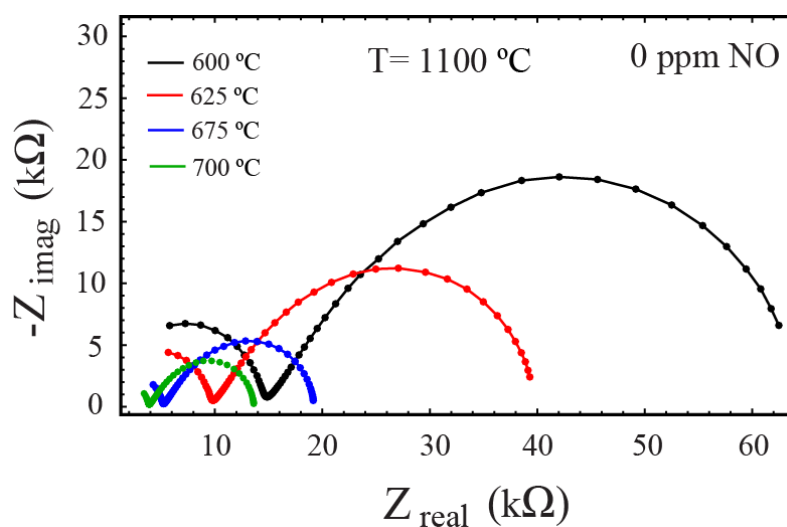
Figure 4-5: Nyquist plot of NO_x sensor fire at 1100℃ without NO and by varying the temperature from 600℃ to 700℃.

Comparing Figure 4-5 to Figure 4-4, we notice that the impedance decreases as the temperature increases, and each curve in Figure 4-5 shows smaller impedance in comparison to the impedance arcs for a sensor fired at 1050℃. The porosity in general

decreased as the firing temperature of the sensor increased and there is a direct relation between the porosity and the impedance of the sensor. Porosity impedes ionic transport as it creates a longer path for the oxygen ions to travel.

Also shown are Nyquist plots with 18% oxygen for the two sensors where the measurements were taken at an operating temperature of 650℃ and (with/without NO) as in Figure 4-6.

The Nyquist plot reveals again by decreasing the porosity of the YSZ by firing the sensor at higher temperature and in our case, the sensor which fire at 1100℃ exhibit lower impedance for both high frequency and low frequency arc and that is with and without NO.
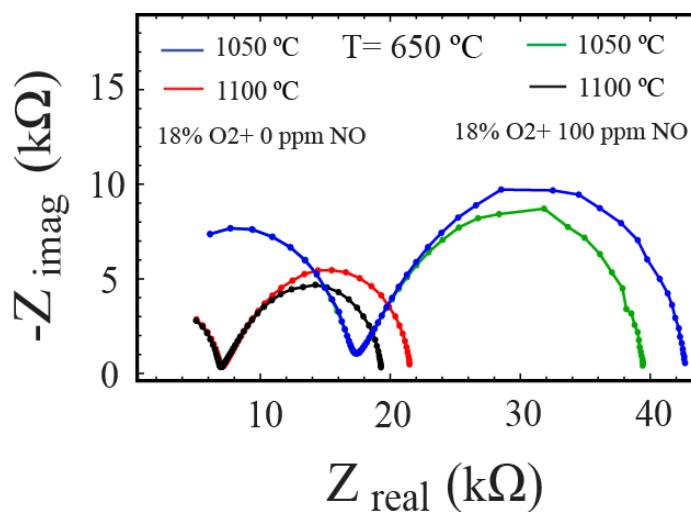
Figure 4-6: Nyquist plots of sensors fired at 1050℃ (blue without No and green with NO) and 1100℃ (Red without NO and black with NO) while operating at 18% O_2 and 650℃.

Moreover, we can see from the figure that the higher oxygen concentration in the background seems to limit the change in the impedance response to NO. Also, applying

NO to the sensors fired at 1050°C and 1100°C decreases the impedance of the lower frequency arc by 3 kΩ.
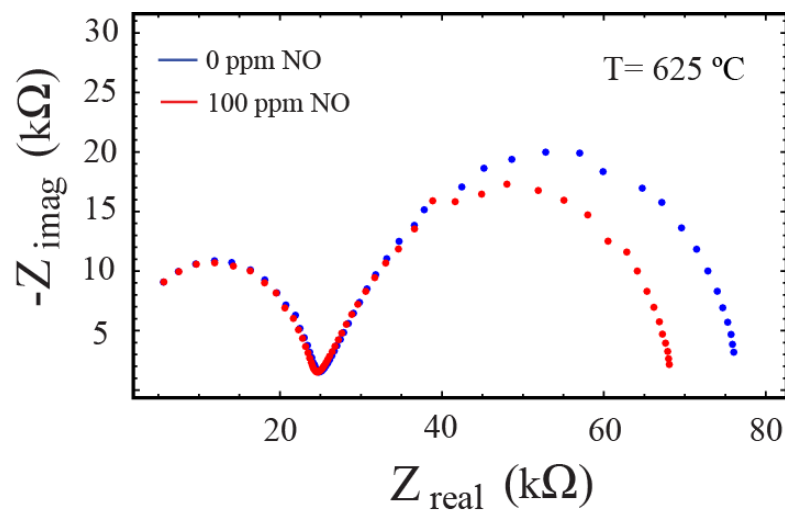
Figure 4-7: Nyquist plot of NO_x sensor fired at 1050°C and at operating temperature 625°C and with 100 ppm NO (red curve) and without NO (blue curve).

In Figure 4-7, we did not notice any change for the impedance of high frequency arc. However, the low frequency arc of the impedance is decreased by applying 100 ppm of NO in comparison to the impedance of the sensor without any flow of NO.
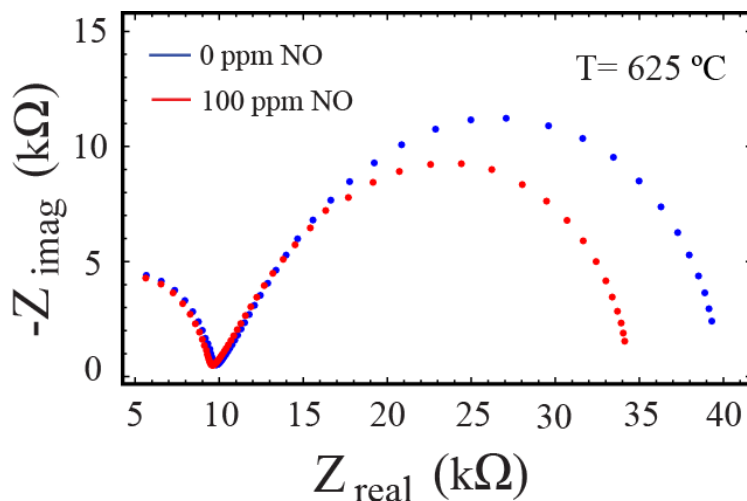
Figure 4-8: Nyquist plot of NO_x sensor fired at 1100℃ and at operating temperature 625℃ and with 100 ppm NO (red) and without NO (blue).

Also Figure 4-8 demonstrates similar results to Figure 4-7 in which the impedance decreases about 7% with a flow of 100 ppm through the sensor compared to the impedance of the sensor without NO in the low frequency arc region.

In comparing Figure 4-8 to Figure 4-7, the impedance is lower for the sensor with the electrolyte fired at higher temperature because the contact between the particles is greater allowing for Oxygen ion conductivity to the triple phase boundary (TPB).

The relative effect of oxygen concentration was investigated on the performance of NO_x sensors fired at 1100℃. The oxygen concentration was varied from 5% to 18%, and the effect on the NO_x sensors represented by the Nyquist plot in Figure 4-9. The increasing of O_2 concentration reduces the size of the low frequency and large frequency. The low frequency arc represents a rate limiting transport process associated with O_2 reduction. This cross sensitivity to O_2 means that NO_x reduction is an intermediate step of the NO_x sensing mechanism [60].
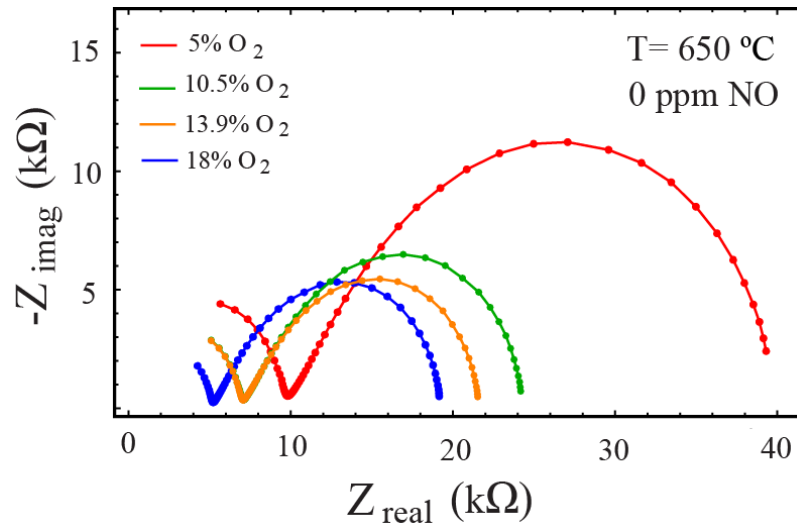
Figure 4-9: Nyquist plot of NO_x sensor fired at T=1100°C by varying the O_2 concertation from 5% to 18% and without adding NO. The flow rate is 100 sccm.

To measure the sensitivity of NO_x and O_2 in the gas sensor, the phase angle can be used.

4.3.2.1 Phase Angle Plot

Phase angle θ or Z_{Phz} is the quantity which represents the lag or the lead of the current response at a specific frequency. The impedance is a complex quantity given as $Z(\omega) = Z_{real} + iZ_{imag}$, which results from the division of alternating voltage $V(t) = V\sin(\omega t)$ over the current response $I(t) = I\sin(\omega t + \theta)$. So, from the complex plane of the impedance and by using the trigonometry, the phase angle can be defined as follows

$$\theta = Z_{Phz} = \tan^{-1}\left(\frac{Z_{imag}}{Z_{real}}\right) \qquad \textbf{Eq. 4-3}$$

The phase angle can be used to measure sensitivity, and it tends to produce a more stable response for detecting NO_x in comparison to monitoring outer impedance components [67], [68]. Oxygen is important for the reaction of NO_x to occur, but there is

often unwanted cross sensitivity of O_2 generated from parallel reactions. Figure 4-10 shows the phase angle as a function of the oxygen concentration at sensor operating frequency of 40 Hz and 20 Hz for a sensor fired at 1100℃. At 40 Hz, the data obtain was similar to the previous work in ref [58]. The oxygen dependence appeared to be similar for the 20 Hz and 40 Hz measurements except for the data collected with 1 to 5% of oxygen. Finally, the data showed that the porous microstructure did not affect the oxygen dependence of the sensor's electrolyte.
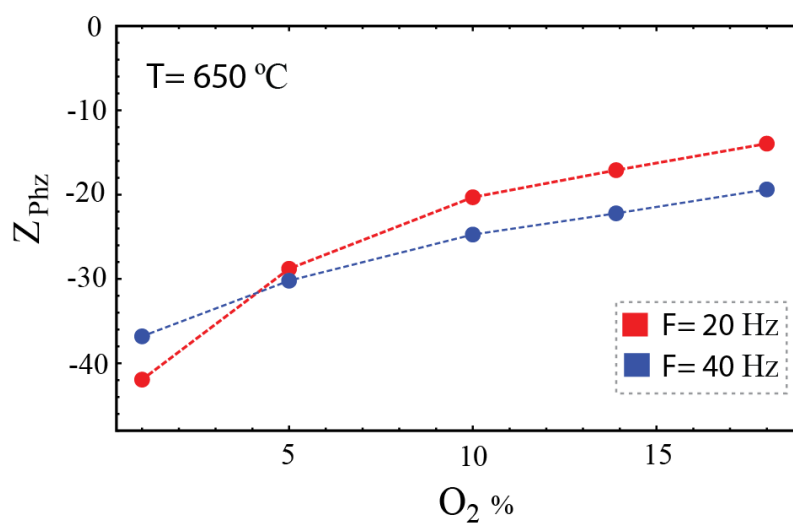
Figure 4-10: Oxygen dependence of sensor fired at 1100℃ measured at two operating frequency 40 Hz and 20 Hz.

CHAPTER 5

CONCLUSIONS AND FUTURE WORK

5.1   Conclusions

Metamaterials are artificial materials designed to provide unique optical properties not found in nature such as magnetism at high frequencies and negative index of refraction. In this thesis, we present comprehensive studies of the magnetic response for two classes of metamaterials (MMs) based on a metallic pair of strips and bowtie resonators immersed in dielectric host material.

To describe the metamaterial designs, analytical theory has developed based on the transmission line and LZ-circuit models. The analytical theory provides an easy to use and clear description of the MMs, revealing the physical mechanism behind the observed magnetic response saturation at high frequencies. While the saturation effects has been known for more than a decade, here we show for the first time that it is a direct consequence of the metal to dielectric transition of the electric response of metals at high frequencies. The theoretical predictions were compared to exact numerical calculations based on the Finite Difference Frequency Domain (FDFD) method revealing an excellent match. The saturation behavior in the magnetic response, occurring within the infrared and optical frequency ranges, and resonators with small (tents of nanometers) sizes is shown to be due

to the capacitive elements. This is contrary to the explanations reported in the literature that rely on empirical modifications of the resonators' inductances.

To map the magnetic resonance saturation, we extensively studied various resonator sizes and configurations. For the microstrip resonators, we found that saturation occurs for resonators with sizes less than 100 nm. Under these conditions, the excitation of magnetic resonances is precluded for frequencies higher than the surface plasma frequency of the system. A similar behavior is observed for the bowtie resonator. However, in this second structure, additional dependencies are manifested and specifically as a function of the slit angle ϕ_0. While an excellent match between the proposed analytical theory and numerical simulations is observed for $\phi_0 < 10°$, further increase of the slit angle is found to result in discrepancies due to fringe effects.

The metallic and semiconductor based pair of strips resonators were implemented in the design of a negative index metamaterials and their optical response was extracted using two commonly used but competing methods: (a) the field averaging method (FAM) and (b) the inverse method (IM). It was shown that negative permeability can be achieved for all microstrip sizes and for both systems under consideration (silver on glass and n-GaAs on glass resonators). However, negative permittivity was obtained only for the silver on glass system and a preset microstrip length. The highest figure of merit (FOM) of -0.9 for the DN-NIM silver on glass system occurred within the frequency range from 5.5 to 7.5 THz. For the metamaterial consisting of n-GaAs on glass microstrip resonators, the highest recorded FOM was -0.5 and within the frequency ranging from 4.5 to 5.4 THz.

Overall, our results show that both extraction methods predict identical magnetic susceptibilities, but under resonance conditions they can deviate when extracting the

electric response of the system. This should serve as a point of caution for the community since both methods are widely used in the literature with little or no attention paid to possible inconsistencies.

For the final project, NO_x sensors were fabricated using a YSZ electrolyte with gold electrodes. The porosity of YSZ electrolyte pellets was studied using two complementary methods, Archimedes measurements and scanning electron microscopy. Both methods verified that the pore size of the electrolyte decreased as the fabrication temperature increased. The range of firing temperature which was used to examine the porosity was (1050℃-1350℃) and was sampled in increments of 50℃.

The next step was to fabricate NO_x sensors by attaching embedded Au electrodes into YSZ electrolytes. Two sensors were fired at 1050℃ and 1100℃ and their performance studied based on the Electrochemical Impedance Spectroscopy (EIS). Nyquist plots were used to examine the influence of the temperature and gas concentration. All of these plots prove that increasing the temperature and O_2 concentration, decreased the impedance as the porosity decreased, and in the case of oxygen, it indicated that the charge of oxygen transported faster which is a necessary step for the NO sensor. However, changing the concentration of NO has an effect only to reduce the impedance of the low frequency arc. Finally, the phase angle at specific frequency (i.e. 40 Hz or 20 Hz) based on the changing of the oxygen concentration was studied for sensor fired at 1100℃. The results show that the sensor is more sensitive to NO in comparison to oxygen.

5.2   Future Work

As a future work, antisymmetric metamaterial designs can be studied including split ring with only one cut or a V-shape designs. In these systems, the quadrupole dipole and

magnetic moments are expected to be suppressed. These moments lead to bi-anisotropic constituent relationships and may be the reason why the inverse and local field averaging methods have diverged for the symmetric metamaterials studied in this thesis.

As future work related to the NO_x sensor, it is desirable to fabricate the NO_x sensor by further increasing the firing temperature which may lead to improved performance. Additionally, we would like to develop a numerical model of the NOx using the Comsol Multiphysics software and compare the simulation results with the experimental results. Such a study may lead to further optimization of the sensor.

APPENDIX A

CALCULATING INDUCTANCE, IMPEDANCE, AND CAPACITANCE OF PARALLEL STRIPS AND BOWTIE MMS

A.1   Parallel Strips MMs

In Section 2.2.1, we require the complex impedance Z_m, capacitance C and inductance L of the parallel strips system. To calculate the impedance Z_m under the assumption $2a \gg d = b$, we consider the inhomogeneous current in the metallic strips due to the skin depth. The electric field in the metal strips is written as

$$\vec{E} = \hat{y}\left(Ae^{ik_m x} + Be^{-ik_m x}\right),$$ **Eq. A-1**

where $k_m = k_0\sqrt{\epsilon_m}$ is the wave vector in the metal. Then the current density is obtained by forcing symmetric boundary conditions at the strips' surfaces leading to

$$\vec{j} = i\omega\epsilon_0\epsilon_m\vec{E}$$

$$= i\omega\epsilon_0\epsilon_m E_0\sec(k_m b)\hat{y}\begin{cases} -\cos[k_m(b+d+x)], & -2b-d \le x \le -d \\ \cos[k_m(b+d-x)], & d \le x \le 2b+d \end{cases}.$$ **Eq. A-2**

Solving for the total current $I = \int j\,da$ flowing through the strips we obtain

$$I = i\omega\epsilon_0\epsilon_m 2bl_z E_0\tanc(k_m b).$$ **Eq. A-3**

Using Eq. (A-3), we write the current density through the total current as

$$\vec{j} = j\hat{y}$$

$$= \frac{I}{2bl_z\text{sinc}(k_mb)}\hat{y}\begin{cases}-\cos[k_m(b+d+x)], & -2b-d \leq x \leq -d \\ \cos[k_m(b+d-x)], & d \leq x \leq 2b+d\end{cases}. \quad \textbf{Eq. A-4}$$

In the transmission line theory, the current is related to the voltage drop $V = 2aE_0$ along the strips through its admittance Y_m as $I = Y_mV$,. Using Eq. (A-3), we obtain the complex valued admittance as

$$Y_m = \frac{1}{Z_m} = \frac{1}{R_m - iX_m} = i\omega\epsilon_0\epsilon_m\left(\frac{2bl_z}{2a}\right)\text{tanc}(k_mb) \quad \textbf{Eq. A-5}$$

where Z_m is the complex impedance, R_m is the real valued resistance and X_m is the real valued reactance. For thin strips $k_mb \leq 1$, we have $Y_m \rightarrow i\omega\epsilon_0\epsilon_mbl_z/a$ as it should be. Finally, the impedance per unit length of the parallel strips system is

$$Z_m = \frac{1}{1/i\omega\epsilon_0\,\epsilon_mbl_z}. \quad \textbf{Eq. A-6}$$

At low frequencies $\epsilon_m \rightarrow i\epsilon_m''$, we recover the classical result

$$Y_m \rightarrow -\omega\epsilon_0\epsilon_m''\frac{bl_z}{a} = \sigma_m\frac{2bl_z}{2a} = \sigma_m\frac{A}{l}$$

where A is the cross sectional of the strip. The capacitance of the parallel strips resonators is also derived using the inhomogeneous electric field profile in the strips Eq. A-1, matched at the boundary with the spacer layer

$$\vec{E}$$

$$= \hat{x}\begin{cases}E_1\sec(k_mb)\cos[k_m(b+d+x)], & -2b-d \leq x \leq -d \quad \textbf{Eq. A-7} \\ E_2, & -d \leq x \leq d \\ E_1\sec(k_mb)\cos[k_m(b+d-x)], & d \leq x \leq 2b+d\end{cases}.$$

Enforcing the boundary conditions (with the field outside being zero), we have

$E_1 = E_3 = \sigma/\varepsilon_m \varepsilon_0$ and $E_2 = \varepsilon_s \varepsilon_0$, where σ is the surface charge density of the strip. Then the electrical field for the system is written as

$$\vec{E} = \hat{y} \frac{\sigma}{\epsilon_0 \epsilon_m} \begin{cases} \dfrac{\cos[k_m(b+d+x)]}{\cos(k_m b)}, & -2b - d \leq x \leq -d \\[2mm] \dfrac{\epsilon_m}{\epsilon_s}, & -d \leq x \leq d \\[2mm] \dfrac{\cos[k_m(b+d-x)]}{\cos(k_m b)}, & d \leq x \leq 2b + d \end{cases} \qquad \textbf{Eq. A-8}$$

and the total potential drop through the system is

$$V = \int_{-d-2b}^{d+2b} |\vec{E}| dx = \left(\frac{d}{\epsilon_0 \epsilon_s a l_z} + \frac{2b}{\epsilon_0 \epsilon_m a l_z} \mathrm{tanc}(k_m b) \right) Q$$

$$\qquad\qquad \textbf{Eq. A-9}$$

$$= \left(\frac{1}{C_s} + \frac{1}{C_m} \right) Q .$$

Then, using the relationship $Q = CV$ we obtain the total capacitance of the parallel plates resonators as

$$C = \frac{C_s C_m}{C_s + C_m} = \epsilon_0 \epsilon_s \frac{a l_z}{d} \left(1 + \frac{2b\epsilon_s}{d\epsilon_m} \mathrm{tanc}(k_m b) \right)^{-1} . \qquad \textbf{Eq. A-10}$$

For thin strips $k_m b \leq 1$, the capacitance can be simplified as

$$C = \epsilon_0 \epsilon_s \frac{a l_z}{d} \left(1 + \frac{2b\epsilon_s}{d\epsilon_m} \right)^{-1} . \qquad \textbf{Eq. A-11}$$

The inductance L of the parallel strips can be obtained from the current density Eq. A-2 which sets the induced local magnetic field in the system. For TM polarization $\vec{H} = \hat{z} H(x, y)$, the Amperes' law reads

$$\nabla \times \vec{H} = -\hat{y} \frac{\partial H}{\partial x} = \vec{j} . \qquad \textbf{Eq. A-12}$$

Substituting the current density from Eq. A-4 and enforcing the boundary conditions

$H(-d - 2b) = H(d + 2b) = 0$, we obtain $H(x, y)$ field across the structure as

$$\vec{B}(x)$$

$$= \frac{\mu_0 I}{2l_z} \hat{z} \begin{cases} 1 + \dfrac{\sin[k_m(b + d + x)]}{\sin[k_m b]}, & -2b - d \leq x \leq -d \\ 2, & -d \leq x \leq d \\ 1 + \dfrac{\sin[k_m(b + d - x)]}{\sin[k_m b]}, & d \leq x \leq 2b + d \end{cases} . \qquad \textbf{Eq. A-13}$$

The magnetic flux then follows

$$\phi = 2a \int_{-2b-d}^{2b+d} B(x) dx = \mu_0 \frac{4a(b + d)I}{l_z},$$

from which the inductance per unit length is obtained

$$L = \frac{\phi}{I} = \mu_0 \frac{2(b + d)}{l_z}. \qquad \textbf{Eq. A-14}$$

A.2   Bowtie MMs

In Section 2.3.1, we used the complex impedance Z_{BT}, and inductance L of the bowtie system. To calculate the impedance Z_{BT}, we write the electric field inside the metallic elements and the gap in the form of

$$E_{\phi m}(r) = \left(\frac{\varepsilon_s}{\varepsilon_m}\right) A_s r \text{ and } E_{\phi s}(r) = A_s r, \qquad \textbf{Eq. A-15}$$

where we have enforced the discontinuity of the electric field at the interface. The potential drop on the external surface of the bowtie structure is then obtained as

$$V = \int_0^{2\pi - 4\phi_0} E_{\phi m} a d\phi + \int_{-2\phi_0}^{2\phi_0} E_{\phi s} a d\phi, \qquad \textbf{Eq. A-16}$$

giving

$$V = 4\phi_0 a^2 A_s \left(1 + \frac{\varepsilon_s}{\varepsilon_m}\left(\frac{\pi - 2\phi_0}{2\phi_0}\right)\right).$$ **Eq. A-17**

The total current in the gap is

$$I = \int_0^{l_z} dz \int_0^a j_d(r)dr = i\omega\epsilon_0\epsilon_s l_z A_s \frac{a^2}{2},$$ **Eq. A-18**

where the current density is $j_d(r) = i\omega\epsilon_0\epsilon_s E_{\phi s}$, Using Eq. A-17 and Eq. A-18, we obtain

the impedance as

$$Z_{bowtie} = \frac{V}{I} = \frac{8\phi_0}{i\omega\varepsilon_0\varepsilon_s l_z}\left(1 + \frac{\varepsilon_s}{\varepsilon_m}\left(\frac{\pi - 2\phi_0}{2\phi_0}\right)\right).$$ **Eq. A-19**

The inductance of the bowtie resonators is derived from the Ampere's law which

for TM polarization reads

$$\nabla \times \vec{H} = -\frac{\partial H}{\partial r}\hat{\phi} = j_d(r)\hat{\phi}.$$ **Eq. A-20**

Then, the magnetic field intensity can be obtained as

$$H(r) = -\int j_d(r)\, dr = -\frac{I}{l_z}\left(\frac{r}{a}\right)^2.$$ **Eq. A-21**

To obtain the inductance, we then calculate the magnetic flux

$$\phi_B = \mu_0 \int H(r)\, da = -\frac{\pi\mu_0 I}{2l_z}a^2.$$ **Eq. A-22**

Finally, the inductance is

$$L = \frac{|\phi_B|}{I} = \frac{\pi\mu_0}{2l_z}a^2.$$ **Eq. A-23**

BIBLIOGRAPHY

[1]   W. Cai and V. Shalaev, *Optical metamaterials fundamentals and applications*, Springer, New York, 2010.

[2]   Anne F. de Baas, European Commission. Directorate General for Research, *Nanostructured metamaterials exchange between experts in electromagnetics and material science,* EUR-OP, 2010.

[3]   J. B. Pendry, A. J. Holden, D. J. Robbins, and W. J. Stewart, "Magnetism from conductors and enhanced nonlinear phenomena," *IEEE Transactions on Microwave Theory and Techniques*, vol. 47, no. 11, pp. 2075-2084, Nov. 1999.

[4]   S. Linden, C. Enkrich, G. Dolling, M. W. Klein, J Zhou, T. Koschny, C. M. Soukoulis, S. Burger, F. Schmidt, and M. Wegener, "Photonic Metamaterials: Magnetism at Optical Frequencies," *Selected Topics in Quantum Electronics, IEEE Journal of*, vol. 12, no. 6, pp. 1097-1105, Dec. 2006.

[5]   J. Valentine, S. Zhang, T. Zentgraf and X. Zhang, "Development of Bulk Optical Negative Index Fishnet Metamaterials: Achieving a Low-Loss and Broadband Response Through Coupling," in *Proceedings of the IEEE*, vol. 99, no. 10, pp. 1682-1690, Oct. 2011.

[6]   V.M. Shalaev, W. Cai, U.K.Chettiar, H-K. Yuan, A.K. Sarychev, V.P. Drachev, and A.V.Kildishev, "Negative index of refraction in optical metamaterials," *Optics Letters*, vol. 30, no. 24, pp. 3356-3358, Dec. 2005.

[7]   V. Podolskiy, A. Sarychev, and V. Shalaev, "Plasmon modes and negative refraction in metal nanowire composites," *Optics Express*, vol. 11, no. 7, pp. 735-745, Apr. 2003.

[8]   J. Valentine, S. Zhang, T. Zentgraf, E. Ulin-Avila, D. A. Genov, G. Bartal and X. Zhang, "Three-dimensional optical metamaterial with a negative refractive index," *Nature*, vol. 455, no. 7211, pp. 376-379, 2008.

[9] C. M. Soukoulis, J Zhou, T. Koschny, M. Kafesaki and E. N. Economou, "The Science of negative index materials," *Journal of physics: Condensed Matter,* vol. 20, no. 30, pp. 1, July. 2008.

[10] V. M. Shalaev, "Optical negative-index metamaterials," *Nat Photon*, vol. 1, no. 1, pp. 41-48, Jan. 2007.

[11] J. B. Pendry, "Negative Refraction Makes a Perfect Lens," *Physical Review Letters*, vol. 85, no. 18, pp. 3966, Oct. 2000.

[12] X. Zhang, "Applied physics: Extreme light-bending power," *Nature*, vol. 470, no. 7334, pp. 343-344, Feb. 2011.

[13] Z. Wang, F. Cheng, T. Winsor and Y. Liu, "optical chiral metamaterials:a review of the fundamentals, fabrication methods and applications," *Nanotechnology*, vol. 41. no. 27,Spt. 2016.

[14] I. Shadrivov, A. Kozyrev, D. Weide, and Y. Kivshar, "Nonlinear magnetic metamaterials," *Opt. Express,* vol.16,no. 25, pp. 20266-20271, Dec. (2008).

[15] Y. Huang, G. Wen and W. Zhu, "Tunable metamaterials based on ferrites and the applications," *2012 International Workshop on Metamaterials (Meta)*, Nanjing, 2012, pp. 1-4.

[16] H-T Chen1, W. J. Padilla1, J. M. O. Zide, A. C. Gossard, A. J. Taylor and R. D. Averitt, "Active terahertz metamaterial devices." *Nature, vol.* 444, pp.597-600, (2006).

[17] M Durán-Sindreu, J. Naqui, F. Paredes, J. Bonache and F. Martín, "Electrically small resonators for planar metamaterial, microwave circuit and antenna design: a comparative analysis," *Appl. Sci*, vol. *2*, no. 2,pp. 375-395; April. 2012.

[18] S. A. Ramakrishna, "Physics of negative refractive index materials," *Reports on Progress in Physics*, vol. 68, no. 2, pp. 449-521, Feb. 2005.

[19] Numerical methods for metamaterial design, Kenneth Diest, Springer.

[20] J. C. Bose, "On the rotation of plane of polarization of electric waves by a twisted structure." Proc. R. Soc. *London A* 63, 146-152 (1898).

[21] J. C. M. Garnett, "Colours in metal glasses and metal films," *Philos. Trans. R. Soc. London Sect*, vol. 73, no. 1, pp. 443-445, 1904.

[22] Mie G., "Beitra¨ge zur optik tru¨ ber medien, speziell kolloidaler metallo¨sungen," *Ann Phys*, vol. 330, pp. 377–445, 1908.

[23] V. G. Veselago, "The ElectroDynamics of substances with simultaniously negative values of ϵ and µ," *Soviet Physics Uspekhi*, vol. 10, no. 4, pp. 509-514, Apr. 1968

[24] D. Smith, W. Padilla, D. Vier, S. Nemat-Nasser, and S. Schultz, "Composite Medium with Simultaneously Negative Permeability and Permittivity," *Physical Review Letters*, vol. 84, no. 18, pp. 4184-4187, May 2000.

[25] W. J. Padilla, D. N. Basov, and D. R. Smith, "Negative refractive index metamaterials," *Materials Today*, vol. 9, no. 7-8, pp. 28-35, July, 2006.

[26] H. Liu, Y. M. Liu, T. Li, S. M. Wang, S. N. Zhu, and X. Zhang, "Coupled magnetic plasmons in metamaterials," *Phys. Status Solidi B,* vol. 246, no. 7, pp. 1397-1406, Jul. 2009.

[27] J. B. Pendry, A. J. Holden, W. J. Stewart, and I. Youngs, "Extermely low frequency plasmons in metallic Mesostructures," *physical review letters*. Vol.76, no. 25, pp. 4773-4776, 1996.

[28] M. H. Alsaleh, "Electromagnetic metamaterials and negative index of refraction with semiconductors," M.S. thesis, Phys, LTU, Ruston, LA, 2012.

[29] M. Fox, *Optical Properties of Solids*, 1st ed. Oxford University Press, USA, 2002.

[30] R. A. Shelby, D. R. Smith, and S. Schultz, "Experimental Verification of a Negative Index of Refraction," *Science*, vol. 292, no. 5514, pp. 77 -79, Apr. 2001.

[31] R. A. Shelby, D. R. Smith, S. C. Nemat-Nasser, and S. Schultz, "Microwave transmission through a two-dimensional, isotropic, left-handed metamaterial," *Applied Physics Letters*, vol. 78, no. 4, pp. 489, 2001.

[32] T. J. Yen, W. J. Padilla, N. Fang, D. C. Vier, D. R. Smith, J. B. Pendry, D. N. Basov, X. Zhang, "Terahertz Magnetic Response from Artificial Materials," *Science*, vol. 303, no. 5663, pp. 1494 -1496, Mar. 2004.

[33] S. Linden, C. Enrich, M. Wegener, J. Zhou, T. Koschny, and C. M. Soukoulis, "Magnetic Response of Metamaterials at 100 Terahertz," *Science*, vol. 306, no. 5700, pp. 1351 -1353, Nov. 2004.

[34] Y. Liu, and X., Zhang, "Metamaterials: a new frontier of science and technology," *Chem. Soc. Rev,* vol. 40, no. 5 pp. 2494-2507, 2011.

[35] D. Schurig, J. J. Mock, B. J. Justice, S. A. Cummer, J. B. Pendry, A. F. Starr and D. R. Smith, "Metamaterial Electromagnetic Cloak at Microwave Frequencies ," *Science*, vol. 314, pp. 977–980, Oct. 2006.

[36] J. B. Pendry, D. Schurig and D. R. Smith, "Controlling Electromagnetic Fields," *Science*, vol. 312, pp.1780–1782, June. 2006.

[37] C. Kittel, *Introduction to Solid State Physics*, 7th ed. Wiley, 1995.

[38] W. Hayt and J. Buck, *Engineering Electromagnetics*, 7th ed. McGraw-Hill Science/Engineering/Math, 2005.

[39] W. J. Padilla, D. N. Basov, and D. R. Smith, "Negative refractive index metamaterials," *Materials Today*, vol. 9, no. 7-8, pp. 28-35, July-August 2006.

[40] https://www.nde-ed.org/EducationResources/CommunityCollege/MagParticle/Physics/Magnetism.htm

[41] J. B. Pendry, and D. R. Smith, "Reversing light with negative refraction," *physics today*, vol. 57, no. 6, pp. 37-43, 2004.

[42] C. G. Parazzoli, R. B. Greegor, K. Li, B. E. C. Koltenbah, and M. Tanielian, "Experimental verification and simulation of negative index of refraction using Snell's law," *Physical Review Letters*, vol. 90, no. 10, pp. 107401, Mar. 2003.

[43   Y.A. Urzhumov, G. Shvets, "Optical magnetism and negative refraction in plasmonic metamaterials," *Solid state communications*, vol. 146, no. 5–6, pp. 208-220, May. 2008.

[44   A. Ishikawa, T. Tanaka, "Negative magnetic permeability of split ring resonators in the visible light region," *Optics Communications*, vol. 258, no. 2, pp. 300-305, Feb. 2006.

[45] Zhou, J., Koschny, T., Kafesaki, M., Economou, E. N., Pendry, J. B., and Soukoulis, C. M., "Saturation of the Magnetic Response of Split-Ring Resonators at Optical Frequencies," *Physical Review Letters*, vol. 95, 223902 (1-4), 2005.

[46] C. M. Soukoulis, T. Koschny, J. Zhou, M. Kafesaki, and E. N. Economou, "Magnetic response of split ring resonators at terahertz frequencies," *Phys. Stat. Sol (b).* vol. 244, no. 4, pp. 1181-1187, 2007.

[47] G. Shvets, and Y. A. Urzhumov, "Negative index meta-materials based on two-dimensional metallic structures," J. Opt. A: Pure Appl. Opt, vol. 8, no. 4, pp. S122-S130.

[48] Penciu, R. S., Kafesaki, M., Koschny, Th., Economou, E. N. and Soukoulis, C. M., "Magnetic response of nanoscale left-handed metamaterials" *Physical Review B*, vol. 81, no. 235111, pp. 1-11, 2010.

[49] U. K. Chettiar, S. Xiao, A. V. Kildishev, W. Cai, H-K Yuan, V. P. Drachev, and V. M. Shalaev, "Optical metamagnetism and negative- index metamaterials, " *MRS Bulletin*, vol. 33, no. 10, pp. 921-926, 2008.

[50] https://skullsinthestars.com/2009/05/19/what-does-negative-refraction-look-like/ [Accessed 21/9/2018].

[51] U. K. Chettiar, A. V. Kildishev, T. A. Klar, and V. M. Shalaev, "Negative index metamaterial combining magnetic resonators with metal films," *Optics Express*, vol. 14, no. 17, pp. 7872-7877, 2006.

[52] Sihvola, A., 1999. Electromagnetic mixing formulas and applications, The IET, London.

[53] Bergman, D.J., and D. Stroud, 1992. Physical Properties of Macroscopically Inhomogeneous Media, Solid State Phys., 46, 147-269.

[54] W. M. Merrill, R. E. Diaz, M. M. LoRe, M. C. Squires and N. G. Alexopoulos, "Effective medium theories for artificial materials composed of multiple sizes of spherical inclusions in a host continuum," *IEEE transactions on Antennas and Propagation*, pages 142 - 148, Vol. 47, No. 1, 1999.

[55] X. Wang, Y.-H. Ye, C. Zheng, Y. Qin, and T. J. Cui, "Tunable figure of merit for a negative-index metamaterial with a sandwich configuration," *Optics Letters*, vol. 34, no. 22, pp. 3568-3570, Nov. 2009.

[56] D. H. Lee, and W. S. Park, "Extraction of effective permittivity and permeability of periodic metamaterials cells," *Physical Review B*, vol. 51, no. 8, pp. 1824, Aug. 2009.

[57] D. R. Smith, and S. Schultz, "Determination of effective permittivity and permeability of metamaterials from reflection and transmission coefficients," *Physical Review B*, vol. 65, no. 195104, pp. 1, Mar. 2002.

[58] L. Cui, F. Han, W. Dai and E. P. Murray, "Influence of microstructure on the sensing behavior of NOx exhausted gas sensors," *J. Electrochem. Soc*, vol. 161, no. 3, pp. B34-B38, 2014.

[59] https://en.wikipedia.org/wiki/Nitrogen_oxide_sensor [Accessed 23/9/2018]

[60] J. M. Rheaume, A. P. Pisano, "Investigation of an impedancemetric NOx sensor with gold wire working electrodes," *J Solid State Electrochem*, vol. 16, Nov. 2012.

[61] J. M. Rheaume, "Solid state electrochemical sensors for nitrogen oxide (NOx) detection in lean exhausted gases," Ph.D. dissertation, Engineering, UCB, Berkeley, Ca, 2010.

[62] S. Carstens and W. A. Majwski, "NOx sensor," https://www.dieselnet.com/tech/sensors_nox.php [Accessed 23/9/2018]

[63] L. Y. Woo, L. P. Martin, R. S. Glass, W. Wang, S. Jung, R. J. Gorte, E. P. Murray, R. F. Novak, and J. H. Visser, "Effect of Electrode Composition and Microstructure on Impedancemetric Nitric Oxide Sensors Based on YSZ Electrolyte," *J. Electrochem. Soc,* vol.155, no.1, pp. J32-J40, 2007.

[64] T. Striker, V. Ramaswamy, E. N. Armstrong, P. D. Willson, E. D. Wachsman, J. A. Ruud, "Effect of nanocomposite Au-YSZ electrodes on potentiometric sensor response to NO_x and CO," Sensor and Actuators B, vol.181, pp.312-318, 2013.

[65] https://slideplayer.com/slide/10868768/ [Accessed 23/9/2018]

[66] M. C. Steil, F. Thevenot and M. Kleitz, "Densification of Yttria-Stabilized Zirconia Impedance Spectroscopy Analysis," *J. Electrochem. Soc*, pp. 390-398, Vol. 144, No. 1, Jan. 1997.

[67] P. L. Martin, L. Y. Woo and R. S. Glass, "Impedancemetric NOx sensing using YSZ electrolyte and 2O3 composite electrodes," *J. Electrochem. Soc*, vol.154, no.3, p. J97, 2007.

[68] E. P. Murray, R. Novak, D. Kubinski, R. Soltis, J. Visser, L. Y. Woo, L. Marting and R. Glass, " Investigating the stability and accuracy of phase response for NOx sensing 5% Mg- modified LaCrO3," *ECS Transactions*, vol. 6, no. 20, pp.43-62, 2008.